Volume 8
Number 24
21 December 2024
Pages 5611–5952

Sustainable Energy & Fuels

Interdisciplinary research for the development of sustainable energy technologies

rsc.li/sustainable-energy

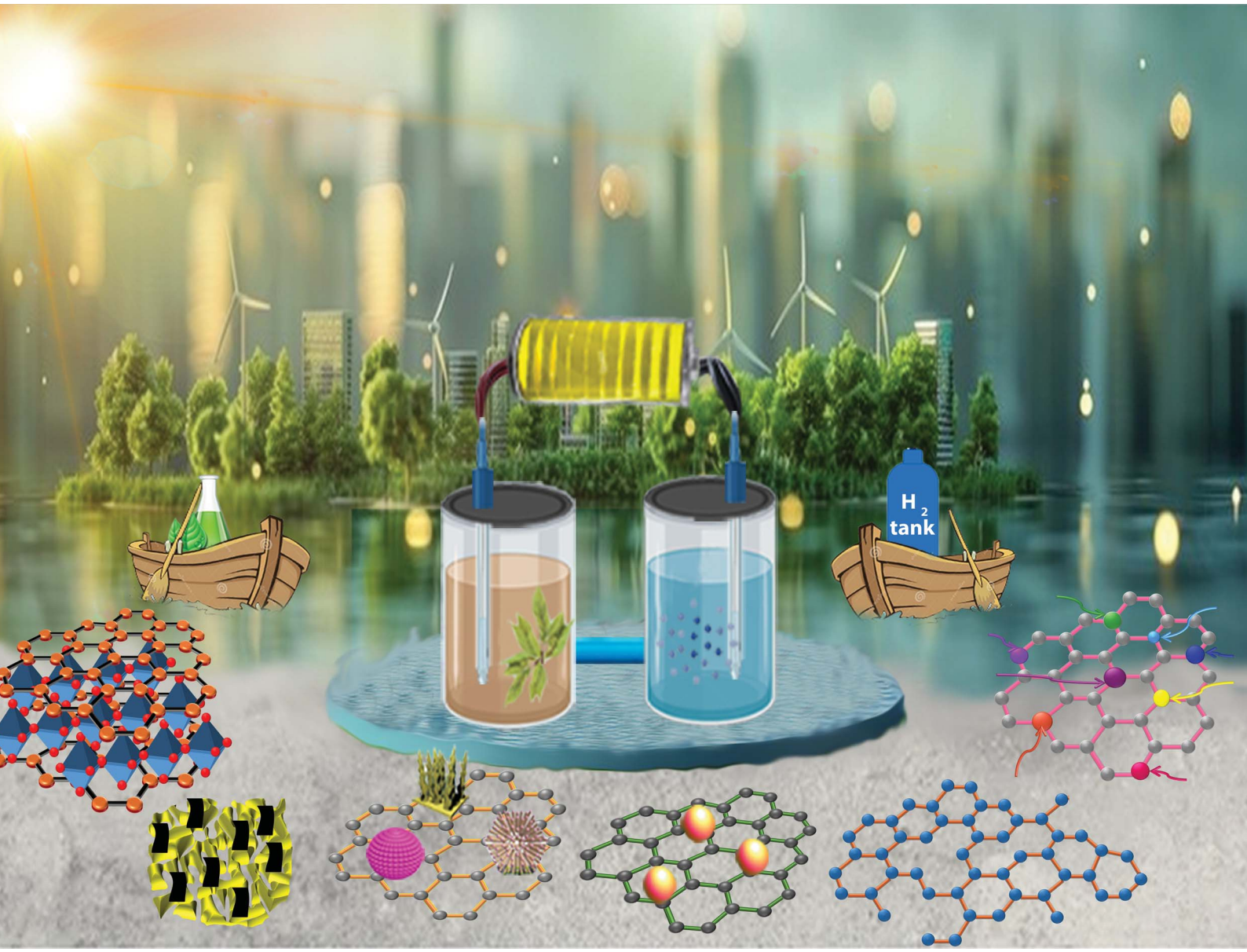

ISSN 2398-4902

ROYAL SOCIETY OF CHEMISTRY

REVIEW ARTICLE

Bahareh Feizi Mohazzab, Dandan Gao *et al.*

Design of nanostructured 2D (photo-)electrocatalysts for biomass valorization coupled with H_2 production

Sustainable Energy & Fuels

ROYAL SOCIETY OF CHEMISTRY

REVIEW

View Article Online
View Journal | View Issue

Cite this: *Sustainable Energy Fuels*, 2024, **8**, 5620

Design of nanostructured 2D (photo-) electrocatalysts for biomass valorization coupled with H_2 production†

Bahareh Feizi Mohazzab,*[a] Kiarash Torabi[b] and Dandan Gao *[a]

Electrocatalytic water splitting driven by renewable energy is a promising strategy for sustainable hydrogen production. However, the slow oxygen evolution reaction (OER) kinetics severely limit the rate of the hydrogen evolution reaction (HER) and the overall energy conversion efficiency of the water electrolyzer. To overcome this challenge, hybrid water electrolysis systems have been developed which replace the sluggish OER with thermodynamically and kinetically favorable biomass (photo-)electro-oxidation. In addition, these systems allow for the simultaneous production of value-added chemical products. This review highlights the design strategies involving the host structure remodeling and structure assembly design of two-dimensional (2D) nanomaterial-based (photo-)electrocatalysts, as well as their wide application in hybrid water electrolysis. Moreover, the current challenges and emerging strategies for the development of advanced (photo-)electrocatalysts and industrial-scale systems are emphasized.

Received 30th July 2024
Accepted 27th September 2024

DOI: 10.1039/d4se01034e

rsc.li/sustainable-energy

1. Introduction

Growing global energy demands and environmental crises have prompted researchers to explore cleaner and more sustainable energy technologies. In this regard, hydrogen (H_2) has been considered as an attractive energy carrier with high gravimetric energy density. In particular, H_2 can be produced in a carbon-neutral fashion and a sustainable energy scheme can be built to this end.[1,2] For example, electrochemical (EC)[3–6] or photo-electrochemical (PEC)[7–9] water splitting has been widely employed for green H_2 production. However, the sluggish oxygen evolution reaction (OER) with a proton-coupled four-electron transfer process is currently the main bottleneck, requiring high voltage supply (>1.8 V *vs.* RHE),[10] suffering from instability of the applied catalyst during operation (*e.g.*,

[a]*Department of Chemistry, Johannes Gutenberg University Mainz, Duesbergweg 10-14, 55128 Mainz, Germany. E-mail: bahareh.feizimohazzab@uni-mainz.de; dandan.gao@uni-mainz.de*

[b]*Department of Materials Engineering and Metallurgy, Faculty of Engineering, Arak University, Arak 3815688349, Iran*

† Electronic supplementary information (ESI) available. See DOI: https://doi.org/10.1039/d4se01034e

Bahareh Feizi Mohazzab

Bahareh Feizi Mohazzab is a dedicated researcher in sustainable energy. She earned her PhD at Bu-Ali Sina University, Iran, focusing on (photo-) electrochemical hydrogen production. Currently, she is a Postdoctoral Fellow (funded by the Alexander von Humboldt Foundation) at the Johannes Gutenberg University of Mainz, under the guidance of Prof. Dr Carsten Streb and Dr Dandan Gao. Her research interests include biomass valorization and sustainable energy production, with the goal of developing efficient technologies for sustainable chemistry and energy to reduce the carbon footprint.

Kiarash Torabi

Kiarash Torabi has a master's degree in Material Science Engineering from Arak University, Iran. His research focuses on the mechanical and structural properties of nanomaterials, specifically investigating phase transformations at the boundaries of heterostructure alloys and nanomaterials. He aims to enhance the understanding of these complex materials to contribute to innovative solutions in sustainable materials and energy.

benchmark IrO_2 OER catalyst degradation under harsh alkaline or acidic conditions[11,12]), and thus preventing large-scale industrial deployment. In consequence, conventional water splitting for efficient H_2 production with economic and ecological viability remains a challenge.[13,14]

One approach to overcome this challenge is hybrid water electrolysis. In this context, the hydrogen evolution reaction (HER) can be alternatively coupled with industrially important (photo-)electro-oxidation reactions, which can produce high-value products while requiring lower overpotentials as compared to the OER. Over the last decade, this novel concept has thrived, and led to major breakthroughs for (photo-)electro-oxidation of organics, including alcohols,[15,16] aldehydes,[17,18] carboxylic acids,[19,20] amines,[21,22] ammonia,[23,24] and hydrazine.[25,26] In addition, biomass feedstock valorization is one of the most attractive (photo-)electro-oxidation reactions.[27,28] For example, 5-hydroxymethyl furfural (HMF), which possesses different functional groups such as a furan ring, aldehyde group, and hydroxymethyl group, can also be valorized to chemicals and fuels with higher values (for details see the ESI, Fig. S1a†). In this regard, furandicarboxylic acid (FDCA) is one of the desired products, which is an important alternative to petroleum-derived terephthalic acid in the polymer industry.[29] Moreover, glucose is considered as another ideal biomass feedstock, which is a waste product generated in the pulp and paper processing industry.[30] For this reason, glucose oxidation is emerging as an industrially important valorization strategy for value-added products, such as gluconic acid (GLA), glucaric acid (GUA), formic acid (FA), tartaric acid and glycolic acid (ESI, Fig. S1b†). Another example, lignin, as one of the most abundant biomass feedstocks, can be converted into value-added products through photocatalysis, EC and PEC, under oxidative conditions.[31] During the oxidation process, functional groups and chemical bonds of lignin can be oxidized through different pathways, including side-chain linkages, aromatic rings, and phenolic hydroxyl groups (ESI, Fig. S2†).[32] Altogether, to give an overview of the biomass and its valorization involved in this review, a summary table is included in the ESI (Table S1).†

The establishment of sustainable systems for simultaneous H_2 production and biomass valorization requires the exploration of low-cost and robust (photo-)electrocatalysts with high performance, including superior intrinsic catalytic activity, excellent selectivity and outstanding durability.[33,34] In this context, two-dimensional (2D) nanomaterials have become an attractive class of (photo-)electrocatalysts which combine a variety of desirable properties including high surface area, high electrical conductivity and tunable reactivity.[35] Triggered by the pioneering studies on graphene and graphene exfoliation, a multitude of 2D layered nanomaterials have been developed, including transition metal dichalcogenides (TMDs), metal oxides, metal organic frameworks (MOFs), layered double hydroxides (LDHs), transition metal carbides/nitrides (MXenes), and hexagonal boron nitride (h-BN).[36,37] The emergence of 2D nanomaterials with unique electrochemical and electronic properties has sparked research interest in biomass valorization coupled with H_2 production. In order to endow 2D nanomaterials with further improved catalytic performance, a wide range of design strategies have been developed including heterojunctions of two distinct materials, structure manipulation (*e.g.* doping and defect/vacancy engineering), and rational integration of 2D nanomaterials on three-dimensional (3D) supports.[33,38]

Herein, this review reports recent developments in the field of 2D nanomaterials for hybrid water electrolysis (Fig. 1). Rational 2D nanomaterial design strategies are reviewed from host structure remodeling (heteroatom doping, defect/vacancy engineering, and co-catalyst engineering) to structure assembly design (construction of heterostructures, surface engineering, and 2D nanomaterials integrated into 3D matrices). Each design strategy is followed by a review of (photo-)electro-oxidation of HMF, glucose, and lignin coupled with H_2 production. Additionally, current challenges and emerging research directions have been pointed out.

Dandan Gao

Dandan Gao is a junior research group leader and Walter Benjamin Fellow (funded by DFG) at the Department of Chemistry, Johannes Gutenberg University Mainz. She received her BSc in materials chemistry from the Ocean University of China, China, and her MSc in Metal Materials Engineering from Shandong University, China. In 2021, she completed her PhD (supervisor: Prof. Dr Carsten Streb) at Ulm University. Her current research is focused on exploring robust electrocatalytic materials for efficient energy conversion/storage, and revealing the catalytic mechanisms at both atomic and molecular levels. She is also developing advanced devices for sustainable water purification.

2. 2D nanomaterials: design strategies and applications in hybrid water electrolysis

2.1. Host structure remodeling

2.1.1. Heteroatom doping. In general, doped nanostructures can be formed by replacing a specific atom in the support structure with another appropriate atom (known as a dopant atom).[41] Heteroatom doping modifies materials' properties by introducing dopants that alter electronegativity, valency, coordination, conductivity and band structure.[42,43] Furthermore, doping can adjust the balance between the electronegativity and bond energy, creating potential active sites and therefore enhancing the material's reactivity.[44]

For PEC applications, in the case of semiconductors, doping is able to enhance the light absorption optical range by multiple methods such as (1) introducing mid-gap states, (2) narrowing band gaps and (3) forming impurity bands.[45] Doping introduces

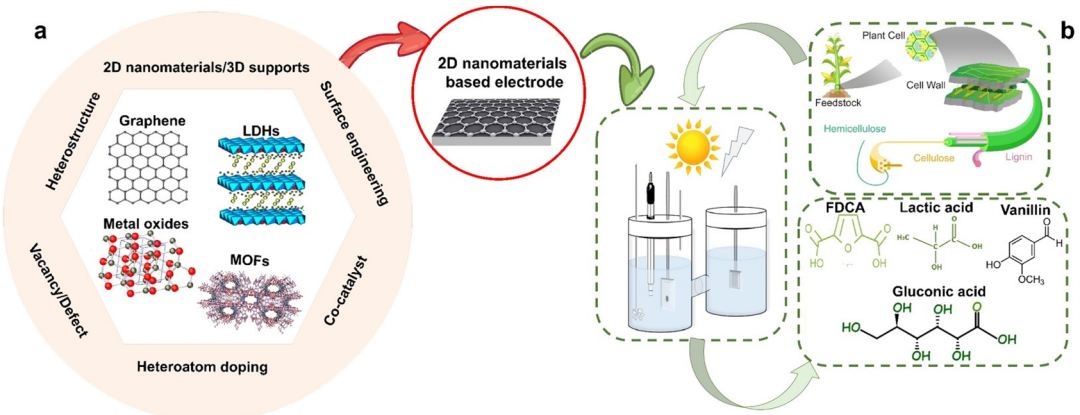

Fig. 1 Graphical illustration of the scope of this review: (a) 2D nanomaterial categories and design strategies and (b) employment of 2D nanomaterials in hybrid water (photo-)electrolysis. The 2D nanomaterial categories and lignocellulosic biomass cell wall have been adapted from ref. 39 and 40, with permission from MDPI and Frontiers, copyright 2022, respectively.

mid-gap shallow or deep-level states which broaden the light absorption edge to longer wavelengths.[46] The mid-gap deep-level states contribute to extending light absorption, and these states do not participate in visible-light photocatalytic activity and act as recombination centers mostly due to the lowest mobility of charge carriers.[47] In contrast, the mid-gap shallow-level states are capable of increasing charge carrier diffusion length and mobility.[48] In the case of noble metal doping, such as gold and silver, the semiconductor experiences the localized surface plasmon resonance (LSPR) effect. This LSPR effect results in enhanced light absorption in the near-infrared region which is beneficial for turning light into energy.[49]

For EC applications, in one instructive example, Wei *et al.*[50] designed a Bi-doped Co_3O_4 nanosheet array on Ni foam (BiCoO-NA/NF) for the 5-hydroxymethyl furfural oxidation reaction (HMFOR) coupled with the HER. In the study, complete conversion of HMF to FDCA (faradaic efficiency (FE): 97.7% and yield: 362.5 μmol h^{-1}) and promotion of H_2 production (yield: 7.33 μmol h^{-1}) can be simultaneously achieved at a low cell voltage of 1.3 V. The outstanding electrocatalytic performance is attributed to heteroatom doping which provides fast mass/electron transfer channels and thus reduces the energy consumption. In a related study, Zhang *et al.*[51] synthesized Cu-doped $Ni(OH)_2$ nanosheets ($Ni_{1-x}Cu_x(OH)_2$), in which Cu presented an island-like elemental distribution (Fig. 2a). The optimum Cu doping led to $Ni_{0.9}Cu_{0.1}(OH)_2$, deriving higher performance toward the HMFOR in comparison to the OER (Fig. 2b). Particularly, $Ni_{0.9}Cu_{0.1}(OH)_2$ realized the HMFOR to FDCA with a 91.2% FE at 1.45 V *vs.* RHE. The high selectivity for the HMFOR is attributed to the formation of more active Ni^{3+} species and the coordination of unsaturated amorphous Cu species which are OER inert.

In addition, Li *et al.*[52] investigated the glucose oxidation reaction (GOR) coupled with the HER over cobalt nanoparticles supported on N-doped porous carbon (Co@NPC-T, T: calcination temperature, Fig. 2c and d). The activity of Co@NPC-800 was evaluated in a two-electrode cell, in which the presence of glucose resulted in a reduced cell voltage, for example, by 180 mV at a current density of 10 mA cm^{-2} (Fig. 2e). Product analysis indicated that lactic acid (LA) and FA were the primary GOR products, with smaller amounts of GLA and GUA. According to DFT calculations, N doping improved glucose adsorption and optimized H_2O adsorption, thereby promoting GOR and HER performance. Furthermore, Li *et al.*[53] synthesized bifunctional Fe-doped Ni_2P nanosheets hybridized with C on Ni foam (Fe–Ni_2P@C/NF) for the GOR and HER (Fig. 2f and g). Additionally, the chronoamperometry experiments conducted on the two-electrode electrolyzer with glucose addition showed that the current decreased to around half of its initial level after 24 h, indicating sustained glucose conversion during electrolysis (Fig. 2h). The electrode showed sustained stability for 24 h and achieved a high current density of 100 mA cm^{-2} at a cell voltage of *ca.* 1.55 V. The electrolysis resulted in complete glucose conversion to LA and FA with a yield of 52.1% and 35.6%, respectively. A high FE of 98.2% for the HER was observed in the hybrid water electrolysis system. DFT calculation indicated that Fe doping optimized the adsorption energy of H_2O molecules and the free energy of H_2 adsorption which facilitates the HER performance.

Moreover, heteroatom doping has also been widely applied for the lignin oxidation reaction (LOR). For example, Cui *et al.*[54] reported the use of a single atom Pt catalyst anchored on an N-doped carbon nanotube (Pt_1/N-CNTs) anode for selective electrocatalytic C–C bond cleavage in lignin, coupled with promoted H_2 production on a glassy carbon cathode. The Pt_1/N-CNTs exhibit unique electronic structures due to the increase in unsaturated coordination number, resulting in the increased active site number. Remarkably, the high dispersion degree of the Pt single atom improved atomic utilization, leading to the increased activity per unit catalyst. Altogether, the Pt_1/N-CNTs demonstrate outstanding selectivity in lignin electrochemical oxidative cleavage of C–C bonds for aromatic monomer formation. In a related study, Hao *et al.*[55] employed an electrochemical redox ion, $[Fe(CN)_6]^{3-}$, in a PbO_2 matrix by the electrodeposition method. The $[Fe(CN)_6]^{3-}$ doped PbO_2 electrode

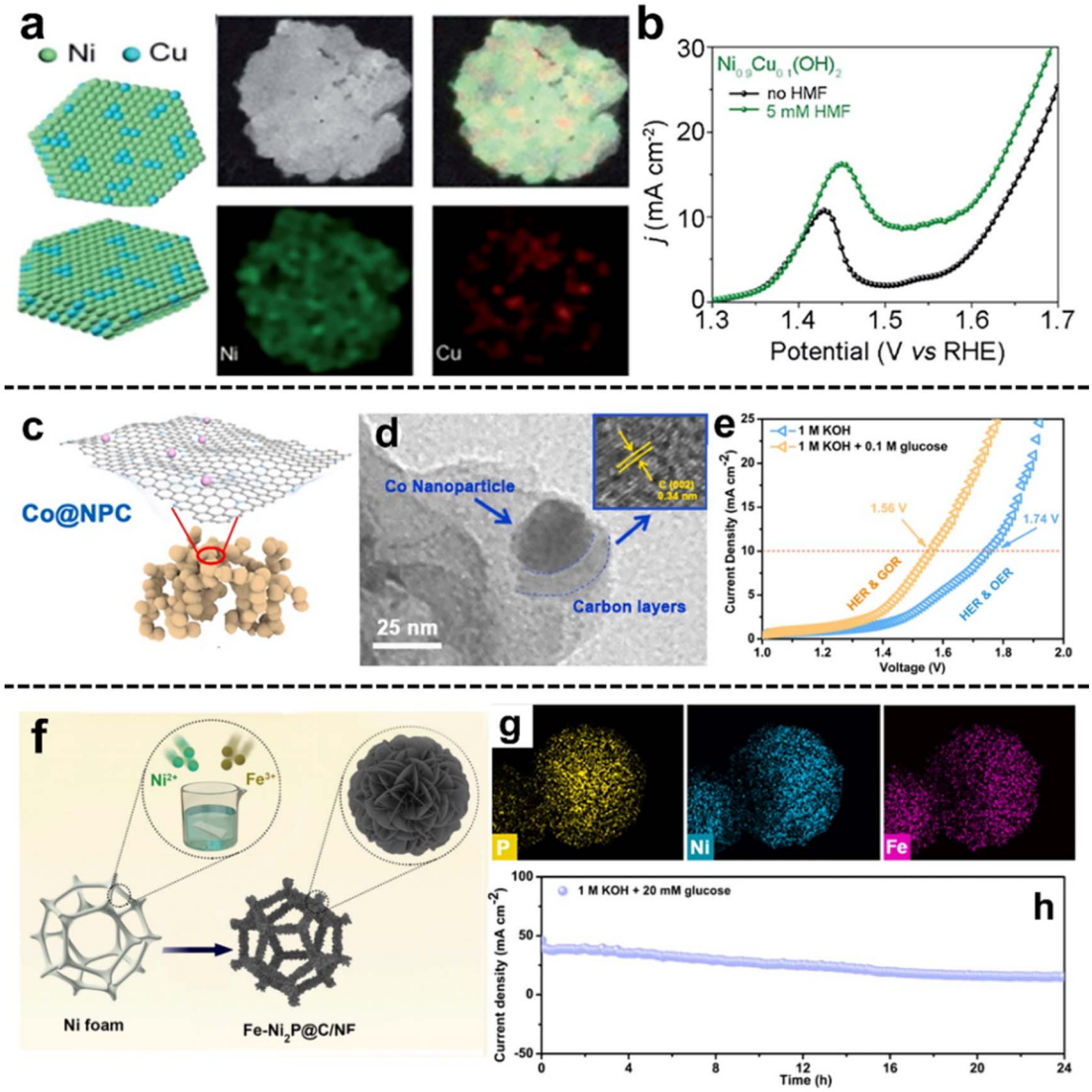

Fig. 2 Selected examples for the Heteroatom doping subsection: (a) schematic illustration of the $Ni_{1-x}Cu_x(OH)_2$ nanosheets and elemental distribution, (b) LSV curve comparison of $Ni_{0.9}Cu_{0.1}(OH)_2$ with and without HMF (these figures have been reproduced from ref. 51 with permission from Royal Society of Chemistry, copyright 2021), (c) the schematic illustration and (d) TEM images of Co@NPC, (e) LSV curves of Co@NPC for the GOR and OER coupled with the HER (these figures have been reproduced from ref. 52 with permission from Elsevier, copyright 2021), (f) the schematic representation and (g) elemental distribution of the Fe–Ni_2P@C/NF electrode, and (h) the chronopotentiometry curve of Fe–Ni_2P@C/NF||Fe–Ni_2P@C/NF in 1 M KOH with 20 mM glucose (these figures have been reproduced from ref. 53 with permission from Elsevier, copyright 2022).

exhibits a service lifetime of 287.25 hours, nearly triple that of standard PbO_2, and a 45% higher rate of alkali lignin degradation. This is attributed to a more compact surface and larger grain size, resulting in increased average cross-sectional area of pores. These structural improvements lead to greater stability and a higher electrochemical active surface area, enabling more efficient reactions. This pioneering work opens a new avenue for next-generation 2D electrocatalyst design for robust lignin electrolysis.

2.1.2. Defect/vacancy engineering. Defect engineering is known to enhance catalytic activity from structural destruction by modulating the electronic and surface properties of catalysts. And the defects obtained can be dimensionally classified into four categories (ESI, Fig. S3a†):[56] (i) point defects, resulted from introducing vacancy/doping and reconstruction of the structure, (ii) line defects, attributed to the dislocation of atoms in the host structure, (iii) planar defects, generated from lattice deviation along the in-plane direction, and (iv) volume defects, led by spatial lattice disorder in the whole body phase. Notably, these categories influence 2D nanomaterial properties in different ways. For example, point defects alter the local electronic and reactive properties, while line defects affect the structural and mechanical properties by disrupting the symmetry and continuity. Furthermore, planar and volume defects can drastically alter the properties of 2D materials *via* inducing phase transitions, changing the dimensionality, and

creating hybrid structures. In particular, point defects have been widely applied to modify 2D nanomaterials owing to their ability to locally tune the physical and chemical properties of catalysts.[57,58]

In the PEC pathway, defects can be located in the bulk phase or on the surface of semiconductors, resulting in volume and planar defects, respectively. They affect the photo-electrocatalytic process in different ways (ESI, Fig. S3b†). For instance, planar defects within the photo-electrocatalyst can act as traps for holes, enhancing charge separation by preventing immediate recombination with electrons. These trapped holes can then react with electron donors on the catalyst's surface, leading to the desired chemical reactions. Conversely, volume defects may trap both electrons and holes, potentially leading to recombination, which is counterproductive for photo-electrocatalytic activity.[59] Therefore, the generated charge carriers could be trapped by volume or planar defects, resulting in recombination or reaction participation, respectively.[60] It should be noted that excessive vacancies can reduce reaction efficiency resulting from unfavourable charge carrier recombination. Therefore, moderate vacancies in 2D nanomaterial design are desired to rationalize visible light absorption, electron–hole pair generation, and hydrogen adsorption.[61]

For applications, Zhang *et al.*[62] developed a series of ternary NiVW layered metal hydroxide electrocatalysts with abundant lattice vacancies ($NiVW_v$-LMH) for the HMFOR (Fig. 3a). Remarkably, the $NiVW_v$-LMH nanosheets obtained lattice-disordered phases and vacancies after 50 cyclic voltammetry (CV) cycles (Fig. 3b), and demonstrated a high current density of 193 mA cm^{-2} for the HMFOR to FDCA with a 100% conversion rate at 1.43 V *vs.* RHE (Fig. 3c). The high performance is attributed to the dissolution of V and W which changes the local coordination of Ni cations and increases the amount of unsaturated active sites. In another study, Zhu *et al.*[63] synthesized a $CuMn_2O_4$ spinel electrocatalyst for the HMFOR using the hydrothermal deposition approach followed by ammonia etching to create oxygen vacancies. The ammonia-etched $CuMn_2O_4$ achieved a current density of 20 mA cm^{-2} at 1.31 V *vs.* RHE. A 100% conversion rate and 96% selectivity to FDCA were observed. Moreover, Tian *et al.*[64] studied PEC hybrid water electrolysis using single-atom Pt on defective TiO_2 nanorod arrays (Pt/def-TiO_2 RNAs) for the GOR coupled with the HER (Fig. 3d and e). The prepared Pt/def-TiO_2 RNAs reached a high photocurrent density of 1.91 mA cm^{-2} at 0.6 V *vs.* RHE (Fig. 3f). After 5.5 h of the GOR, 98.8% of glucose was converted into GLU and GLA with a yield of 84.3% and 9.2%, respectively. And a high FE of 99% was observed for the HER. The TiO_2 defective structure led by oxygen vacancies promotes charge dynamics for the PEC GOR by facilitating charge movement. def-TiO_2 possesses a large electron conduction band and large surface band bending which are favorable properties for charge carrier movement and extraction.

2.1.3. Co-catalyst engineering. Coating the catalyst surface with a co-catalyst is a prominent tool to boost the catalytic activity. The co-catalysts participate in electrochemical oxidation/reduction by providing active sites for the reactions between charge carriers and intermediate ions (*e.g.* H^+ or OH^-).

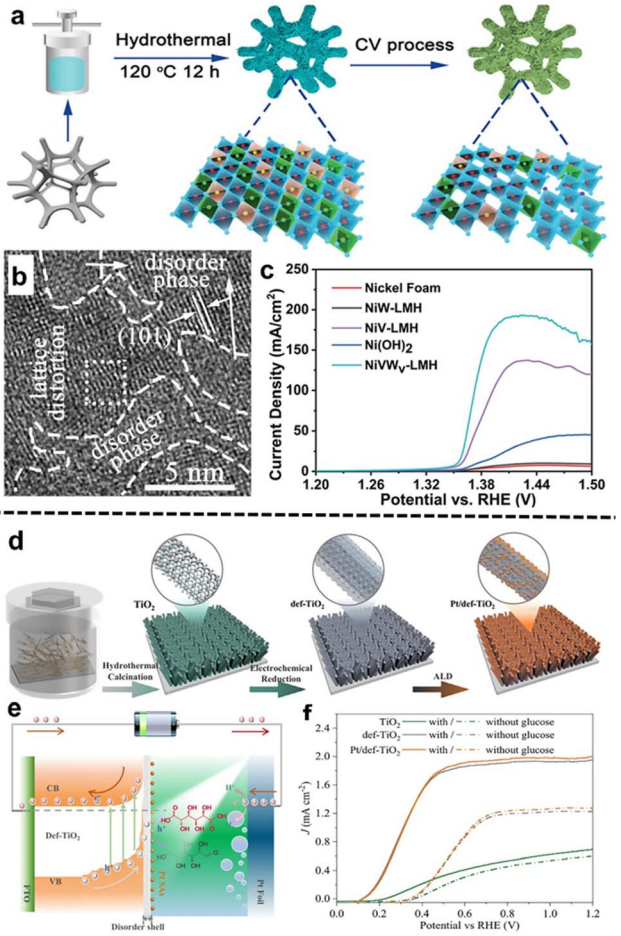

Fig. 3 Selected examples for the Defect/vacancy engineering subsection: (a) synthetic route of $NiVW_v$-LMH crumpled nanosheets, (b) HR-TEM image of $NiVW_v$-LMH, and (c) LSV curves of $NiVW_v$-LMH after the 50th CV cycle with 90% *iR* correction (these figures have been reproduced from ref. 62 with permission from Wiley, copyright 2023), (d) fabrication process for the TiO_2, def-TiO_2, and Pt/def-TiO_2 NRAs, (e) energy band diagram of the Pt/def-TiO_2 NRA photoanode and charge carrier movement during GOR and HER processes, and (f) LSV profiles of prepared photoanodes for the GOR under AM 1.5G, 100 mW cm^{-2} illumination (these figures have been reproduced from ref. 63 with permission from Nature, copyright 2023).

In order to enhance overall water (photo-)electrolysis performance, Rh, Pt, Ru, and Ir metals and oxides of Fe, Co, Ir, Ru, and Ni have been utilized as co-catalysts for the HER and OER, respectively.[65]

In PEC systems, the integration of a co-catalyst is crucial for promoting charge separation and enhancing transport at the semiconductor–co-catalyst interface.[66] The addition of the co-catalyst leads to the formation of a space-charge region, which in turn establishes a semiconductor/co-catalyst junction, commonly referred to as a Schottky barrier.[67] At this junction, the alignment of Fermi energy levels initiates electron migration. The direction of electron movement and the resultant band bending are influenced by the relative Fermi levels of the materials in contact. Typically, for an n-type semiconductor combined with a metal co-catalyst possessing a higher work

function, there is a flow of electrons from the semiconductor to the metal. This electron flow induces upward band bending, propelling electrons toward the space-charge region, while holes tend to accumulate on the photo-electrocatalyst's surface.[68] The formation of the Schottky barrier is instrumental in mitigating electron–hole recombination, thereby significantly improving PEC efficiency. It is essential to recognize that the precise direction of electron flow and band bending is contingent upon the specific energy levels of the materials involved (ESI, Fig. S3c†). Despite the high activity of noble metals, earth-abundant 2D noble-metal-free co-catalysts have emerged in recent years attributed to the low cost, tunable composition, superior structural stability and tailorable reactivity.[69]

Liang *et al.*[70] employed Ni_3N–V_2O_3 as a potent co-catalyst for the HMFOR-assisted HER (Fig. 4a), which demonstrated high FDCA selectivity (98.7%) and yield (96.1%) as well as advanced HER performance (Fig. 4b and c). Co-catalyst engineering altered the electronic structure and reduced the band gap energy, leading to low cell voltage (1.40 V at 10 mA cm^{-2}) and 100% FE of the HER in hybrid water electrolysis. For GOR application, Ru and Ir nanoclusters and their oxides have been extensively employed due to their structural and chemical stability, as well as their superior electrocatalytic activity. For example, Chen's group[71] developed a novel calixarene-based $\{Ni_{18}\}$ coordination wheel entity (CIAC-123) as an efficient bifunctional electrocatalyst for the GOR and HER (Fig. 4d). Promisingly, the open-wheel structure can serve as a template for encapsulation and fabrication of tiny metal nanoclusters such as Au, Pd, Ir, Ru, Rh, Pt, and AuPd. As observed, CIAC-123 was performed as an efficient catalyst for the GOR while bimetallic AuPd@CIAC-123 exhibited significantly improved HER performance (Fig. 4e and f). Considering the pore diameter (0.9 nm) in AuPd@CIAC-123 and glucose molecule diameter (~1 nm), it could be concluded that the presence of AuPd limits the accessibility of the inner cavity to glucose molecules, while hydrogen ions can pass through the cavity for absorbance. Therefore, based on the size of molecules, the Ni sites are responsible for the GOR while HER activity can be attributed to Pd sites with synergistic effects of Au and Ni.

Co-catalyst engineering has also been employed to explore advanced catalysts for efficient LOR. In this regard, Rauber *et al.*[72] coated a third metal (Mn, Pd, V, or Ti) in mixed Ru–Ir oxides ($Ru_{0.2}Mn_{0.2}Ir_{0.6}O_x$, $Ru_{0.2}Pd_{0.2}Ir_{0.6}O_x$, $Ru_{0.2}V_{0.2}Ir_{0.6}O_x$ and $Ru_{0.2}Ti_{0.2}Ir_{0.6}O_x$). Compared to the initial binary metal oxide ($Ru_{0.4}Ir_{0.6}O_x$), the co-existence of the third metal, particularly for Mn metal, can significantly improve the yield of monomers from the LOR. In one related investigation, the Gao group modified the NiFeO arrays fabricated on Ni foam with Ir single atoms (Ir–NiFeO@NF) for efficient 1-phenylethanol (a simple lignin model) valorization and H_2 production.[73] This showed that deployment of bifunctional Ir–NiFeO@NF in a two-electrode cell can reach a current density of 10 mA cm^{-2} at 1.33 V. Additionally, a H_2 production rate of *ca.* 0.45 mmol h^{-1} cm^{-2} was observed with a FE close to 100% at an applied cell voltage of 1.5 V. Anodic product analysis revealed that lignin motifs were transformed into benzoic acids.

2.2. Structure assembly design

2.2.1. Construction of heterostructures. Heterostructures are structures in which different components are linked together by heterogeneous interfaces or heterojunctions (*e.g.*, semiconductor-carbon nanomaterials).[74,75] The design of heterostructures can alter the number of active sites, lattice strain, and electronic structure due to interfacial changes.[76,77] In particular, a modulated electronic structure can enhance the adsorption/desorption of catalyst reaction intermediates, thereby increasing the electrocatalytic activity.[78] Furthermore, it is well documented that a larger contact area can accelerate the charge carrier movement and create sufficient transport channels at the interfaces of heterostructures.[79] Remarkably, heterostructures with various dimensions exhibit diverse interfacial contacts such as point contact (0D–2D), line contact (1D–2D) and face contact (2D–2D).[79] Among them, the face contact in 2D–2D heterostructures is an ideal condition to re-localize electrons and improve redox ability.[80] Details about the contact interfaces of synergistic nanostructures as well as synthetic methodologies have been previously reviewed.[81,82]

For PEC applications, primary objectives of heterostructure design are to prevent charge recombination while promoting charge movement and separating electron–hole pairs using diverse charge transfer mechanisms. The efficiency of PEC processes is enhanced through improved charge-carrier separation, enriched active sites, and optimized reaction conditions facilitated by heterostructure design.[83] Based on the position of the conduction band (CB) and valence band (VB), these mechanisms are often categorized into five groups: p–n junction, type I, type II, Z-scheme and S-scheme.[7,8,84,85] Notably, the charge transfer mechanism differs when incorporating carbon-based materials into the photo-electrocatalyst heterostructure.[68] For instance, when a graphene-based heterostructure is irradiated with light, the semiconductor generates charge carriers, which then transfer electrons from the CB of the semiconductor to the graphene sheets, resulting in a reduction reaction. Meanwhile, the remaining holes in the VB of the semiconductor participate in oxidation reactions. A schematic of the charge transfer mechanism of graphene-semiconductors is available in ESI, Fig. S3d.†

In (photo-)electrocatalysis, heterostructure design provides the (photo-)electrocatalyst with high surface area and strong interfacial contact. In this context, the charge carriers generated during the reaction can be quickly and efficiently transported away from the active sites, thus enhancing the overall reaction rate. As a prime example, Sun *et al.*[86] investigated the coupling of the HMFOR and HER using a heterostructured nanorod array electrocatalyst deposited on Ni foam ($Ni/Ni_{0.2}Mo_{0.8}N/NF$), which demonstrated excellent activity toward both the HMFOR and HER. Remarkably, the hybrid water electrolysis system employing the bifunctional $Ni/Ni_{0.2}Mo_{0.8}N/NF$ electrode only required 1.51 V for a current density of 50 mA cm^{-2}. And product analysis showed 98.5% yield for FDCA. This superior performance was attributed to electronic structure modulation and robust contact between the Ni foam support and $Ni_{0.2}Mo_{0.8}N$. In another example by Zhong *et al.*,[87] Ni_xSe_y

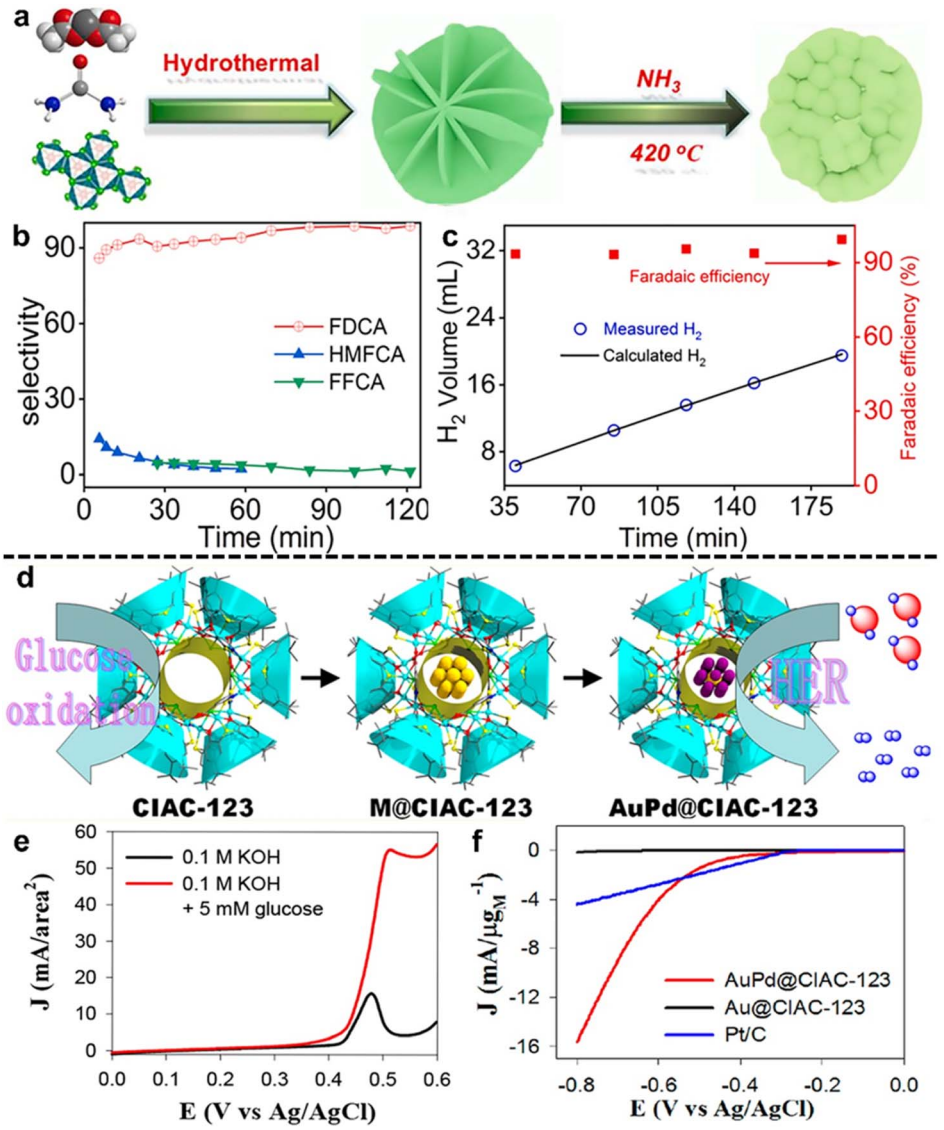

Fig. 4 Selected examples for the Co-catalyst engineering subsection: (a) synthetic route of the Ni_3N–V_2O_3 electrode, (b) HMFOR selectivity for FDCA, HMFCA and FFCA, (c) hydrogen production and faradaic efficiency for the HER as a function of electric charge (left axis) and electric current (right axis) (these figures have been reproduced from ref. 70 with permission from Elsevier, copyright 2021), (d) schematic illustration of the wheel structure of CIAC-123, M@CIAC-123, and AuPd@CIAC-123; M: tiny metal nanoclusters such as Au, Pd, Ir, Ru, Rh, Pt, and AuPd, (e) LSV curves of CIAC-123 in 0.1 M KOH with or without 5 mM glucose, and (f) LSV curves of AuPd@CIAC-123, Au@CIAC-123, and commercial Pt/C in 0.5 M H_2SO_4 for the HER (these figures have been reproduced from ref. 71 with permission from American Chemical Society, copyright 2018).

nanowire arrays covered with NiFe LDH nanosheets (named Ni_xSe_y–NiFe LDH@NF) were applied for the HMFOR coupled with the HER on Pt sheets. In the reported heterostructured Ni_xSe_y–NiFe LDH@NF, a Ni_xSe_y nanowire core facilitated fast charge transfer while NiFe LDH nanosheets provided a large surface area with abundant active sites (Fig. 5a and b). To this end, the HMFOR activity of Ni_xSe_y–NiFe LDH@NF was significantly promoted, leading to substantially reduced overpotentials as compared to the presented reference materials (Fig. 5c). In addition, a high yield of 99.3% and FE of 98.9% were observed for the HMFOR to FDCA at 1.42 V *vs.* RHE. Moreover, Deng *et al.*[88] modified copper sulfide core nanowires grown on Cu foam with NiCo-layered double hydroxide outer-shell nanoarrays (Cu_xS@$Ni_{0.75}Co_{0.25}O_xH_y$/CF) for simultaneous HMFOR and HER (Fig. 5d–f). The hybrid electrolysis system only required a cell voltage of 1.34 V to reach 10 mA cm^{-2}, which is lower than that of the HMF-absent system by 0.27 V (Fig. 5g). Notably, Cu_xS@$Ni_{0.75}Co_{0.25}O_xH_y$/CF achieved complete HMF conversion to FDCA with 100% FE at 1.3 V *vs.* RHE and a unity FE for the HER. The open core–shell structure of nanoarrays provided a large number of active sites, which facilitated mass transfer. Furthermore, the incorporation of Co adjusted the electronic structure of Ni to a higher content of Ni^{3+}, which accelerated the adsorption of reactants and intermediates. The synergetic effect between the designed specific nanostructure

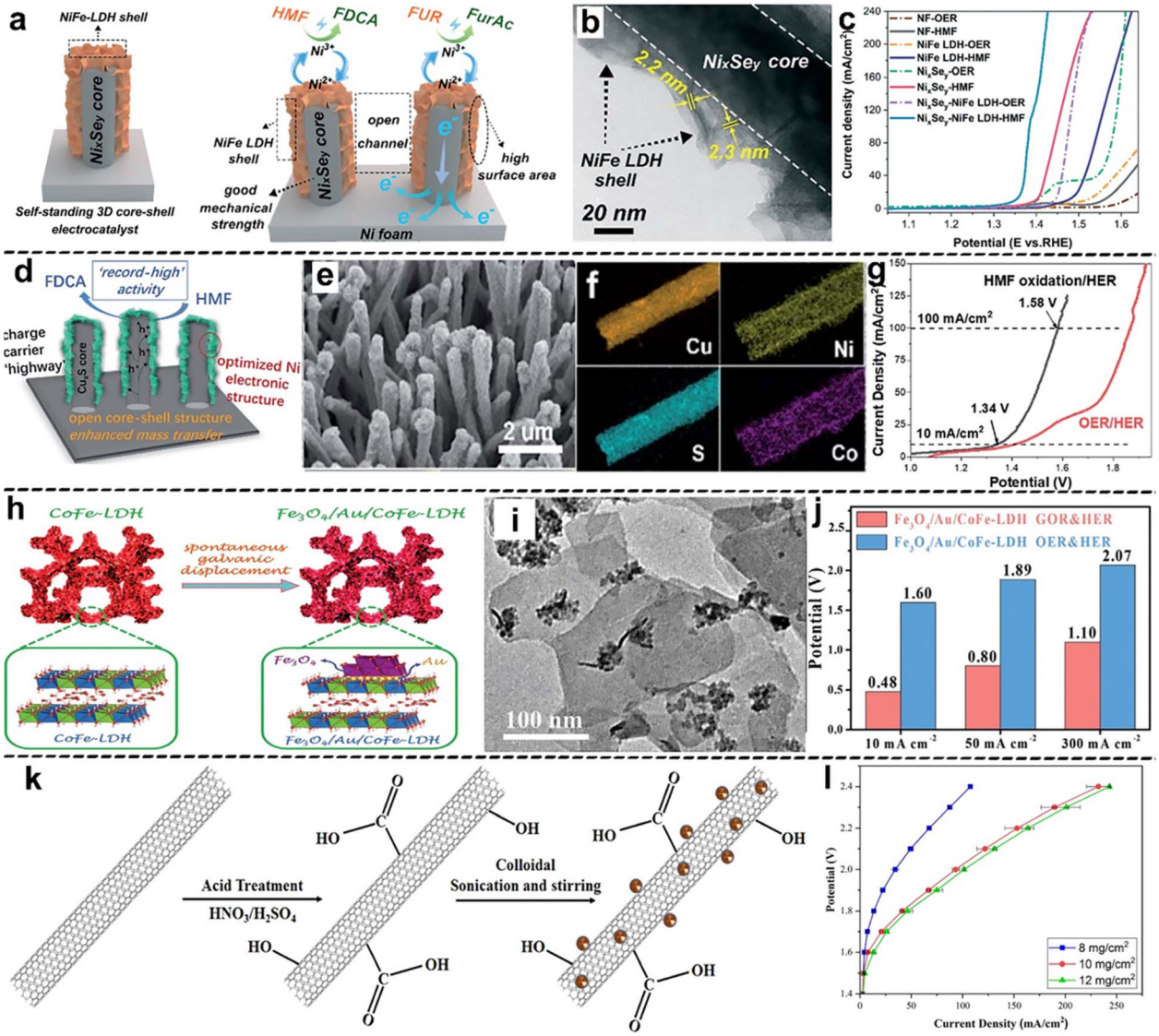

Fig. 5 Selected examples for the Construction of heterostructures subsection: (a) the schematic structure and the mechanism proposed for the electrooxidation of HMF and furfural (FUR) on the Ni_xSe_y–NiFe LDH@NF electrode, (b) TEM images of the Ni_xSe_y–NiFe LDH core–shell structure, (c) LSV curves of NF, NiFe LDH@NF, Ni_xSe_y@NF and Ni_xSe_y–NiFe LDH@NF (these figures have been reproduced from ref. 87 with permission from Royal Society of Chemistry, copyright 2022), (d) schematic illustration, (e) SEM image and (f) elemental mapping of Cu_xS@$Ni_{0.75}Co_{0.25}O_xH_y$/CF, (g) LSV curves for the OER/HER and HMFOR/HER over the bifunctional Cu_xS@$Ni_{0.75}Co_{0.25}O_xH_y$/CF electrode (these figures have been reproduced from ref. 88 with permission from Royal Society of Chemistry, copyright 2020), (h) synthetic route and (i) TEM image of CoFe-LDH and Fe_3O_4/Au/CoFe-LDH, (j) cell potential of the GOR/HER and OER/HER at different current densities with *iR*-compensation (these figures have been reproduced from ref. 89 with permission from Wiley, copyright 2021), (k) synthetic approach for PbO_2/MWNTs for the LOR, and (l) LSV curve from different PbO_2/MWNT catalyst loading samples (these figures have been reproduced from ref. 90 with permission from IOP Publishing, copyright 2019).

and modulated electronic structure is beneficial for the improved performance.

In addition, Sun *et al.*[89] designed hetero-nanoparticles (Fe_3O_4/Au) distributed on the basal plane of CoFe-LDH, leading to Fe_3O_4/Au/CoFe-LDH with heterostructures for efficient GOR coupled with the HER (Fig. 5h and i). This study highlighted that the presence of Fe_3O_4 and CoFe-LDH in the sandwich structure boosted the electrochemical activity of Au nanoparticles in the GOR by regulating its electronic structure and providing a large surface area. In this context, the Fe_3O_4/Au/CoFe-LDH heterostructures displayed significantly reduced cell voltages for the GOR/HER compared to the OER/HER (Fig. 5j). In particular, a current density of 50 mA cm^{-2} led to full conversion of glucose to gluconate and the HER with a FE of *ca.* 99.6%. Moreover, Bateni *et al.*[90] integrated PbO_2 nanoparticles into high surface area multi-walled carbon nanotubes (PbO_2/MWNTs) *via* the impregnation method for the electrochemical LOR (Fig. 5k), which showed boosted rates in terms of both the LOR and HER (on a Pt black cathode) in a lignin electrolysis cell. Additionally, the comparison of current densities at the same

potential shows that increasing the catalyst loading from 8 to 10 mg cm^{-2} significantly enhanced the performance due to the change in the number of accessible active sites (Fig. 5l), while a further increase in catalyst loading (12 mg cm^{-2}) cannot yield higher performance. In another study, the electroactivity of a NiCo electrocatalyst was improved towards lignin-assisted water electrolysis by fabricating a $NiCo/TiO_2$ heterostructure electrocatalyst as an anode and Pt nanoparticles loaded on a carbon cloth as a cathode.[91] The results showed that at a cell voltage of 1.6 V, the current density and the FE of H_2 evolution reached 10 mA cm^{-2} and 99%, respectively. Furthermore, the gas product analysis revealed 100% purity of H_2.

2.2.2. Surface engineering. As aforementioned in the heterostructure design strategy, highly efficient catalyst interfaces render promoted electrocatalytic performance. In this context, surface morphology and wettability are considered as crucial parameters. Compared to smooth surfaces, micro- and nanostructured catalyst surfaces are able to expose more active sites, shorten the transport distance of charge carriers, and increase the absorption of light to generate and separate charge carriers by reflection or scattering.[92,93] For example, compared to $BiVO_4$ flat films, adjusting the distance between $BiVO_4$ nanospheres to match the incident light wavelength traps and scatter light, can substantially enhance the light-driven capability and interface accessibility (ESI, Fig. S3e†).[94] Furthermore, high wettability is desirable by rational surface engineering, which enables efficient gas bubble release, high utilization of surface active sites and therefore strong interaction between the catalyst interface and electrolyte. For this purpose, superaerophobic and superhydrophilic surface coatings are always built by researchers.[95]

For the applications of the surface engineering design strategy, Deng *et al.*[96] reported hexagonal nanoplatelet-on-nanoarray NiCo hydroxide-based electrocatalysts (t-NiCo-MOF) for the HMFOR coupled with the HER on a $MoNi_4$ cathode (Fig. 6a and b). To achieve a current density of 100 mA cm^{-2}, the t-Ni_1Co_1-MOF||$MoNi_4$ hybrid electrolysis system requires a low cell voltage of 1.392 V, while the HMF-free system requires 1.7 V (Fig. 6c). The product quantification highlighted complete conversion of HMF to FDCA with a high FE of 98%. The high activity and selectivity observed can be attributed to the reasonable morphology design, providing increased interfacial contact and facilitating mass transfer. In a related study, the Wang group[97] developed a bifunctional superhydrophilic/superaerophobic surface by depositing NiS quantum dots (QDs) onto wrinkled N,O,S-tri-doped carbon porous nanosheets (NiS@NOSC) for simultaneous HMFOR and HER (Fig. 6d). Static-water-droplet contact angles and underwater air-bubble contact angles (Fig. 6e) revealed the superhydrophilic and superaerophobic properties of the NiS@NOSC surface, accelerating electrolyte penetration and bubble release, respectively. As compared to the OER/HER system, the HMFOR/HER system exhibited a considerably reduced cell voltage, and only 1.51 V was required for reaching 50 mA cm^{-2} current density (Fig. 6f). Remarkably, 100% conversion of HMF to FDCA was observed with a FE of *ca.* 99.6% and a 100% FE for the HER. In another example, Zhou *et al.*[98] employed pine needle-like Co_3O_4 nanowires on Ni foam (CoNW/NF, Fig. 6g) as an efficient bifunctional electrocatalyst for the HMFOR and HER. Benefiting from the porous nanorod-like leaf surface morphology (Fig. 6h), abundant active sites can be exposed. This led to a reduced cell voltage for the HMF-present system (Fig. 6i). Specifically, after 5.73 h of the HMFOR, complete conversion into FDCA with a yield of 96.8% and a FE of 96.6% was observed, together with a 100% FE for the HER. The outstanding performance is attributed to the open nanowire structures that facilitated mass transfer, while the interconnected structures enhanced the charge transfer process.

Additionally, the Augustynski group[101] proposed a nanostructured WO_3 photoanode for the GOR coupled with the HER, resulting in a variety of valuable products such as GLA, GUA, erythrose and arabinose. In this study, simultaneous GOR and HER at 1.23 V *vs.* RHE demonstrated a high photocurrent density of *ca.* 6.5 mA cm^{-2} under stimulating AM 1.5G illumination. In another example, Wang *et al.*[99] employed ultrafast oxygen plasma to modify commercial Co–Ni foam (CNF) to give CNF-60 a superhydrophilic surface (Fig. 6j) for the GOR and HER. Compared to the pristine CNF, CNF-60 yielded higher current density at applied potentials higher than 1.45 V, suggesting more favorable mass transfer of glucose. In the two-electrode (CNF-60||CNF-60) cell, reduced cell voltages can be observed in the presence of glucose, for example, by 269 mV at a current density of 10 mA cm^{-2} (Fig. 6k). Moreover, water contact angle evaluation of the modified surface and pristine conditions (Fig. 6l) suggested that both materials possess superhydrophilic features. This indicates that the improved electrochemical performance is attributed to elemental changes resulted from the plasma treatment. Furthermore, Ghahremani *et al.*[100] reported the LOR coupled with the HER by co-electrodepositing Ni and Sn on a Ti substrate, leading to the $NiSn_{20\%}$ alloy electrode showing cauliflower-like morphology with increased porosities and channels (Fig. 6m and n). Compared to the lignin-free condition, the obtained $NiSn_{20\%}$ demonstrated higher performance in the lignin-present system (Fig. 6o). Additionally, it delivered a high H_2 production rate of 72 ml h^{-1} at a cell voltage of 1.6 V, while a remarkable target vanillin production rate of 300 g kg per lignin per min was observed at a cell voltage of 1.4 V.

2.2.3. 2D nanomaterials integrated into 3D matrices. The recent development in electrode design has led to the integration of 2D nanomaterials with 3D porous substrates. This can significantly enhance the interfacial contact between the nanomaterials and substrate, thus improving electrical conductivity of resulting electrodes. Furthermore, the diffusion lengths for ions and electrons are effectively reduced, facilitating more efficient and direct pathways for charge transport and storage.[102–104] In this context, a variety of aligning orientations can be achieved including horizontal, vertical, heterogeneous and arbitrary structures.[35] In particular, metal foams featuring adjustable surface area and tunable surface morphology have been widely applied to integrate 2D nanomaterials for energy conversion and storage systems.[105–110]

For example, Chen and coworkers[111] proposed electrochemically tuning nonporous CoS_x deposited on Co foam to Co_3O_4 (Co_3O_4/CF, Fig. 7a) for the HMFOR and HER. The obtained

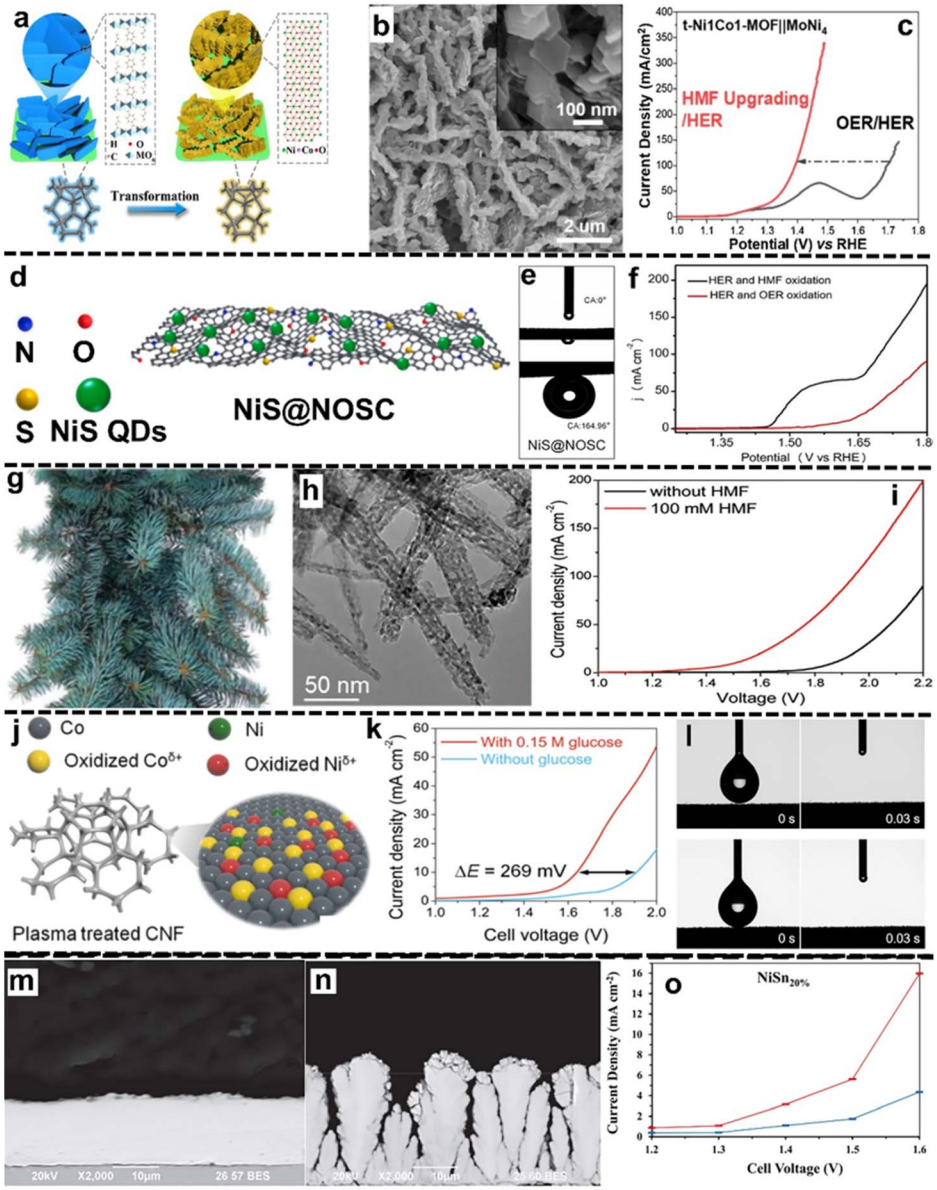

Fig. 6 Selected examples for the Surface engineering subsection: (a) the illustration of a nanoplatelet-on-nanoarray t-NiCo-MOF electrocatalyst deposited on NFs, (b) SEM images of the transformed Ni_1Co_1-MOF (t-Ni_1Co_1-MOF), and (c) LSV curve of the t-Ni_1Co_1-MOF(anode)||$MoNi_4$(cathode) system for the OER/HER and HMFOR/HER (these figures have been reproduced from ref. 96 with permission from Elsevier, copyright 2020), (d) illustration of the synthesis procedure of NiS@NOSC, (e) static-water-droplet contact angles for under-water air-bubble contact angles on the surface of NiS@NOSC, (f) LSV curves of NiS@NOSC||NiS@NOSC for the OER/HER and HMFOR/HER (these figures have been reproduced from ref. 97 with permission from Elsevier, copyright 2022), (g) photo of a pine needle, (h) TEM image of morphological features of the exfoliated CoNWs, (i) LSV curves of the two-electrode system (CoNW/NFs||CoNW/NFs) with and without HMF (these figures have been reproduced from ref. 98 with permission from Royal Society of Chemistry, copyright 2019), (j) schematic illustration of the modification of CNFs *via* O_2 plasma treatment, (k) LSV curve of the CNF-60||CNF-60 system for the GOR coupled with the HER, (l) changes in the wetting behavior of the surface: (top row) pristine CNFs and (down row) CNFs after 60 minutes (CNF-60) of plasma exposure (these figures have been reproduced from ref. 99 with permission from Royal Society of Chemistry, copyright 2023), (n) cross-section image of Ni (m) and $NiSn_{20\%}$, and (o) current density as a function of cell voltages for $NiSn_{20\%}$ in 1 M NaOH solution (absence of lignin: blue plot and presence of lignin: red plot) (these figures have been reproduced from ref. 100 with permission from IOP publishing, copyright 2020).

Co_3O_4/CF exhibits a hierarchical structure consisting of microspheres and nanosheets distributed on the surface (Fig. 7b). The cell voltage was significantly reduced when HMF was present in the hybrid electrolysis system (Fig. 7c). Attributed to defective structures and abundant electroactive sites distributed on the 3D Co foam support, bifunctional Co_3O_4/CF achieved complete conversion of HMF to FDCA with a high yield (93.2%), as well as high FEs for both the HMFOR and HER (92.9% and 99.8%, respectively). Moreover, the Zhao group[112] synthesized a sheet-like cobalt hydroxide-cerium dioxide

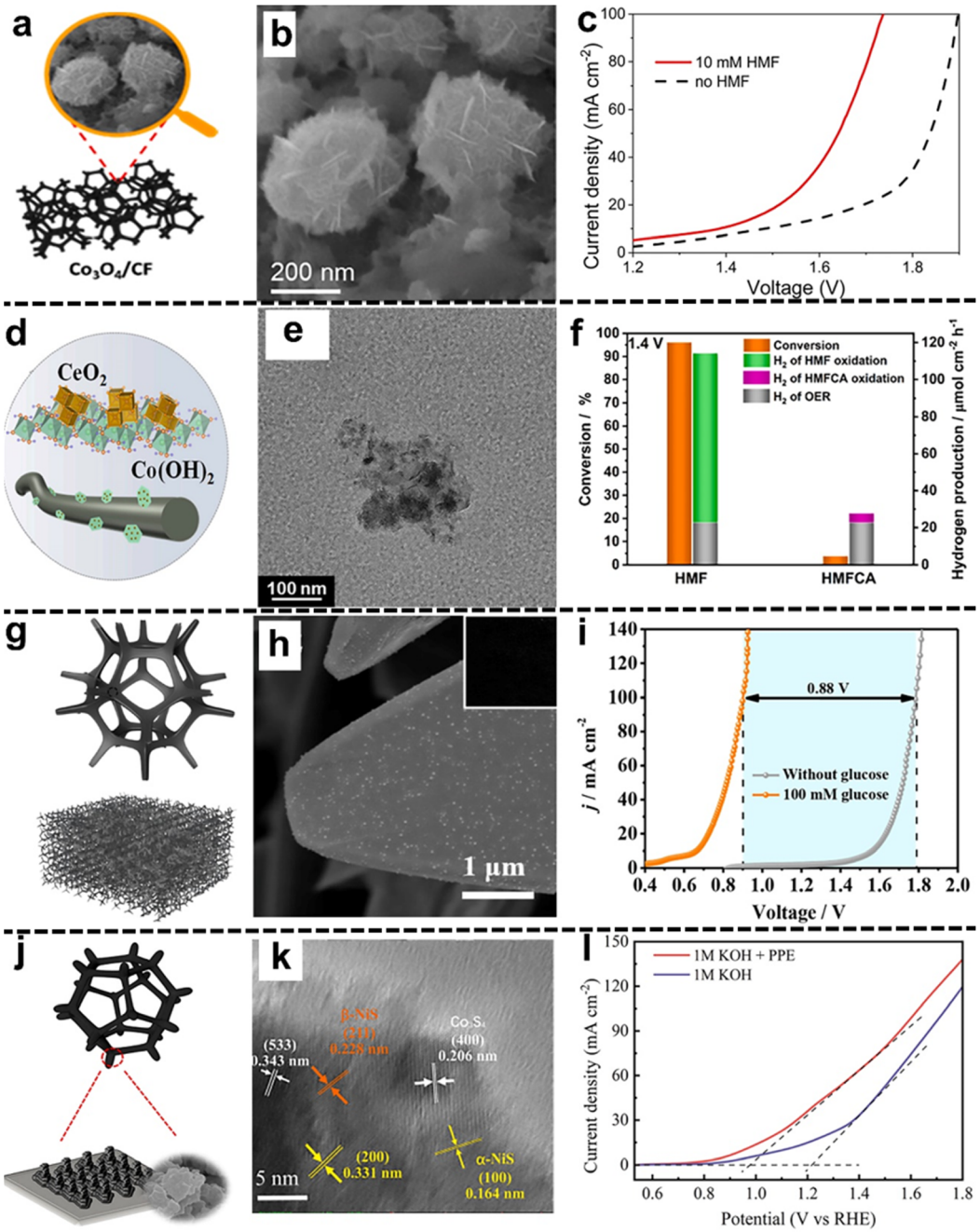

Fig. 7 Selected examples for the 2D nanomaterials integrated into 3D matrices subsection: (a) illustration and (b) SEM image of the fabricated Co_3O_4/CF, (c) LSV curves of the Co_3O_4/CF||Co_3O_4/CF system in the presence and absence of 10 mM HMF (these figures have been reproduced from ref. 111 with permission from Elsevier, copyright 2022), (d) a schematic illustration and (e) TEM images of the $Co(OH)_2$–CeO_2 electrode, (f) the conversion of HMF and HMFCA and corresponding H_2 production at a potential of 1.4 V using the $Co(OH)_2$–CeO_2 electrode (these figures have been reproduced from ref. 112 with permission from Elsevier, copyright 2023), (g) a schematic illustration and (h) SEM image (inset: optical photograph of the sample) of CF@CoNC-2T, (i) LSV curves of a two-electrode cell consisting of CF@CoNC-2T||CF@CoNC-2T with and without glucose (these figures have been reproduced from ref. 113 with permission from Royal society of chemistry, copyright 2022), (j) a schematic structure and (k) TEM image of NF@Co_3S_4/(α,β)-NiS, and (l) LSV curves of NF@Co_3S_4/(α,β)-NiS in 1.0 M KOH with and without 1.0 mM PPE (these figures have been reproduced from ref. 114 with permission from Elsevier, copyright 2022).

composite catalyst on carbon fiber paper ($Co(OH)_2$–CeO_2) for the HMFOR coupled with the HER (Fig. 7d and e). Through two-electron oxidation, HMF was converted to 2-furancarboxylic acid (HMFCA) with a selectivity of 89.4% and a yield of 85.8%. Promising hybrid water electrolysis was carried out at 1.4 V with an optimized HMF conversion rate (96%) and boosted H_2 production rate (114.39 μmol cm^{-2} h^{-1}, Fig. 7f). In addition, Xin *et al.*[113] anchored bifunctional size-controllable Co/Ni-co-doped carbon on Cu foam (CF@CoNC-*x*T, *x* represents the crystallization times) for the GOR and HER (Fig. 7g). The obtained CF@CoNC-2T electrode shows a rough surface with Co nanoparticles distributed (Fig. 7h). The two-electrode cell showed

a cell voltage of only 0.9 V, which is 0.88 V lower than that of the glucose-free system (Fig. 7i). Additionally, a FE of 100% for the HER and value-added products (GNA as well as GRA) was obtained. In another study by Liu and colleagues,[115] $NiFeO_x$ and $NiFeN_x$ were deposited on 3D nickel foam for the GOR and HER, respectively. The optimized electrodes were able to deliver a current density of 200 mA cm^{-2} at a low cell voltage of 1.48 V. Meanwhile, the efficient conversion of glucose to GRA was observed with a high FE of 87% and yield of 83%.

Recently, Ni-based porous electrodes have been extensively developed for the LOR, owing to their low cost, high catalytic activity, and robust anti-corrosion stability.[116] Notably, under oxidative operation, Ni electrodes always form a catalytically active surface NiOOH layer, leading to enhanced lignin conversion performance.[117] In this regard, the Waldvogel group reported a series of studies on the anodic depolymerization of lignin on 2D planar or 3D porous Ni-based electrodes.[118–121] It is reported that the repeated use of Ni foam electrodes for the LOR significantly increased vanillin production, indicating an activation phenomenon from the *in situ* deposition of a modified layer on the electrode surface (ESI, Fig. S4†).[117] In addition, Wang *et al.*[114] fabricated self-supported Co and Ni bimetallic sulfides on Ni foam (NF@Co_3S_4/(α,β)-NiS, Fig. 7j) for the oxidation of 2-phenoxy-1-phenylethanol (PPE), a typical β-O-4 lignin model compound coupled with the Pt catalyzed HER. The structural analysis demonstrates that Co_3S_4 is stacked in a lamellar structure with pore channels which facilitate mass transfer rate (Fig. 7k). At the same current density (*i.e.*, 10 mA cm^{-2}), the potential of PPE oxidation (0.954 V *vs.* RHE) was considerably lower than that of the PPE-free system (*i.e.*, 1.107 V *vs.* RHE, Fig. 7l). Meanwhile, a large amount of H_2 bubbles produced at the cathode was observed.

3. Current challenges and emerging strategies

This review reports on recently developed design strategies for 2D nanomaterial based (photo-)electrocatalysts for biomass valorization coupled with H_2 evolution, of which HMF, glucose and lignin have been exemplified as promising representatives. The long-standing benefits as well as existing limitations of reviewed designed strategies are presented in Table 1. In addition, Table S2† concretely summarizes how a specific design strategy improves the performance of the investigated hybrid water electrolysis systems, in terms of reduced cell voltage, enhanced H_2 production efficiency, and simultaneous access to value-added products. In spite of the progress achieved, bridging the current-generation hybrid water electrolysis systems to the future-advanced ones still requires more efforts. Hence, the following section highlights the current research challenges, as well as pioneering examples of emerging strategies for developing the next generation of robust hybrid water electrolysis systems.

(i) Multiple design strategies for advanced 2D nanomaterials: to date, single design strategies have been widely employed for 2D nanomaterial modification, targeting the promoted activity, selectivity or durability, respectively. To comprehensively improve the catalytic performance of developed 2D nanomaterials, employing multiple design strategies on one material is considered to be a more versatile technique. Here, we have summarized the complementation of reviewed design strategies (Table 1) to guide smarter and more efficient 2D nanomaterial design. In addition, selective design strategies for anode and cathode materials should be applied in a compatible manner so as to boost biomass valorization as well as H_2 production simultaneously, while bifunctional design strategies are highly desired to simplify the material fabrication and avoid cross-contamination under oxidative/reductive conditions.

(ii) Comprehensive investigation of catalyst interfaces under operation: it is well known that catalyst interfaces play an important role in governing the catalytic performance in terms of reactivity, selectivity and stability. In this context, a clear understanding of catalyst interfacial processes such as dynamic chemical/structural/electronic evolution, formation/interaction of key electroactive intermediates, and dominant reaction pathways, is required to rationalize the selection of design strategies and to drive the knowledge-based development of next-generation biomass valorization/HER electrocatalysts.

Combination of (photo-)electrochemical and cutting-edge *in situ* characterization techniques under operation can offer valuable insights at atomic- and molecular-levels to this end, leading to the emergence of a wide range of *in situ* microscopic and spectroscopic methods, such as surface interrogation-scanning electrochemical microscopy (SI-SECM) for quantitative information of surface adsorbates,[132–134] transmission electron microscopy (TEM) for dynamic structural and morphological evolution at the nano-/atomic-scale,[135] Fourier transform infrared spectroscopy (FTIR)[63,136,137] and Raman spectroscopy[138–141] for delivering structural information on surface-formed species, surface-bound adsorbates and species in the electrochemical double-layer, vibrational sum-frequency generation (vSFG) for accessing the structure of water molecules at the catalyst/water interface without bulk signal contribution,[142–144] X-ray absorption spectroscopy (XAS) for capturing the transformations of the local chemistry of the probed element, *e.g.*, precise information on the electronic structure, bond length, oxidation state, and coordination environment under operation,[145–148] X-ray diffraction (XRD) for tracking crystal structure and phase transitions,[149,150] and X-ray photoelectron spectroscopy (XPS) for surface elemental composition and oxidation state alteration under operation.[151,152]

In addition to these milestones, facilitating the use of machine-learning methods for theoretical calculation is a versatile approach for in-depth kinetic modeling of the focused catalyst interfaces, which can be used to predict the reaction mechanism by calculating the energy levels of the electrons in the catalytic material and the interactions between the electrons and the ions in the electrolyte.[153–156]

(iii) (Photo-)electrocatalyst recycling and regeneration: under harsh catalytic conditions, the degradation of catalytic performance in terms of activity, selectivity and durability, is always

Table 1 A summary of the benefits, limitations and complementation of the reviewed design strategies in biomass valorization coupled with H_2 production

Design strategies	Benefits	Limitations	Complementary strategies
Host structure remodeling[122–127]			
Heteroatom doping	• Enhance catalytic activity	• Difficult to control the distribution of heteroatoms uniformly	• Surface engineering and integration of 2D nanomaterials into 3D matrices: ensure uniform dispersion of doped heteroatoms
	• Tailor electronic properties and surface chemistry	• Complex synthesis processes	• Defect/vacancy engineering: simplifies the synthesis process as defect/vacancy sites can facilitate the incorporation of heteroatoms
Defect/vacancy engineering	• Creates more active sites	• Excessive defects may compromise structural integrity	• Heteroatom doping: mitigates the risk of compromising integrity by stabilizing the structure
	• Improves reaction kinetics	• Difficult to control defect density	• Construction of heterostructures: reduces the impact of excessive defects by providing additional mechanical support
			• Surface engineering: maintains the uniformity of defect density by functionalizing the surface with specific properties
Co-catalyst engineering	• Enables synergistic effects with the host material	• Possible leaching of co-catalysts	• Heteroatom doping and defect/vacancy engineering: reduces the risk of leaching by creating more robust active sites
	• Enhances selectivity and efficiency	• Higher cost due to multiple components	• Construction of heterostructures: simplifies the integration process by providing a more stable structure
		• Complexity of selection and integration of suitable co-catalysts	• Integration of 2D nanomaterials into 3D matrices: addresses the complexity of selection and integration by providing a more stable structure
Structure assembly design[38,128–131]			
Construction of heterostructures	• Enhances charge separation	• Complex fabrication	• Surface engineering: achieves uniform integration and simplifies the fabrication process
	• Improves catalytic performance	• Potential stability issues under specific reaction conditions	• Heteroatom doping and defect/vacancy engineering: addresses stability issues by improving the interaction between different components
	• Synergistic effects between different components		• Integration of 2D nanomaterials into 3D matrices: increases stability by improving the mechanical stability
Surface engineering	• Improves catalytic selectivity	• Requires precise control	• Heteroatom doping and defect/vacancy engineering: achieves uniform surface coverage and reduces contamination by stabilizing functional groups as anchoring points and improving the interaction with reactants
	• Increases surface area	• Potential for surface contamination	• Construction of heterostructures and integration of 2D nanomaterials into 3D matrices: reduces the risk of contamination and improves uniform surface coverage
	• Enhances interaction with reactants	• Ununiform surface coverage	
Integration of 2D nanomaterials into 3D matrices	• High surface area	• Unstable immobilization	• Construction of heterostructures and surface engineering: facilitates better immobilization and reduces aggregation by improving the interaction ability
	• Unique electronic properties	• Potential aggregation issues	• Heteroatom doping and defect/vacancy engineering: achieves uniform dispersion and reduces aggregation by introducing more reactive sites on the 2D nanomaterials
	• Enables efficient charge transport and mass transfer	• Ununiform dispersion and alignment of 2D materials in a 3D matrix	• Co-catalysts: improves alignment within the 3D matrices by the synergistic effect with the 2D nanomaterials

difficult to predict and/or prevent. Even the improper handling of the deactivated (photo-)electrocatalysts has caused serious implications, including waste generation and resource depletion.[157] To this end, reactive element recycling and sustained performance regeneration of the aging catalyst are essential for environmental and economic relevance, which is however limited not only by high cost, but also high energy consumption.[158–161] Notably, the lifespan of 2D nanomaterial-based (photo-)electrocatalysts can be extended in more eco-friendly modes,[162,163] like employing green synthesis methods (*e.g.* grinding, milling, and laser-assisted methods) or an electrochemical activation approach. More remarkably, to re-attain superior performance, they can be re-modified by considerate design strategies[164] summarized in this review.

(iv) Strategically bridging the lab-scale to the industrial-scale: despite significant progress in the design and fabrication of highly efficient 2D nanomaterials, there is still a gap between the laboratory scale and industrial scale for advanced biomass valorization coupled with H_2 production.[165,166] On one hand, low-cost manufacturing and scaling up approaches of 2D

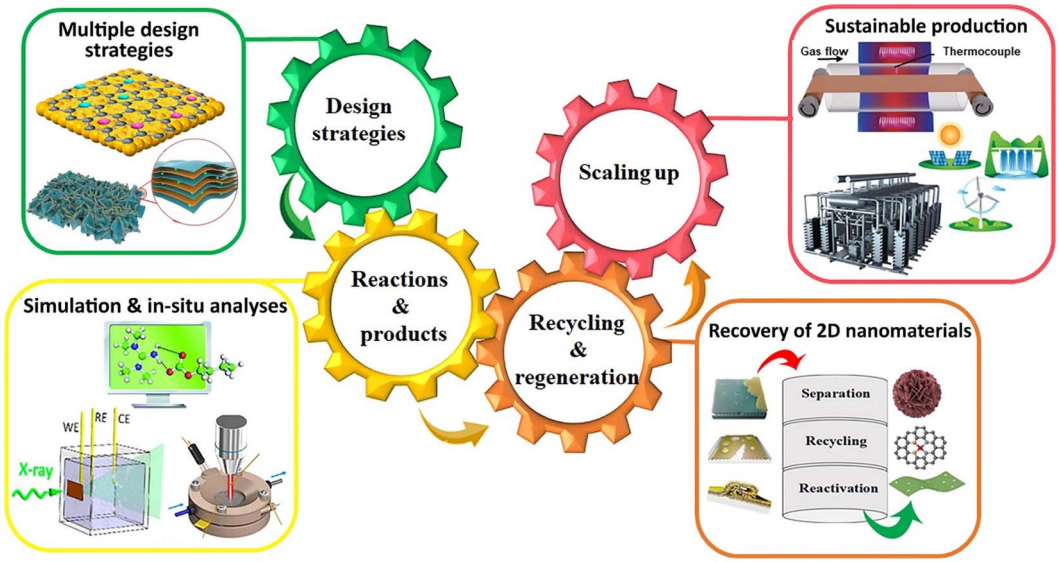

Fig. 8 A schematic representation of current challenges and suggested solutions.

nanomaterials should be developed to this end.[167] As an instructive example, roll-to-roll chemical vapor deposition (CVD) reactors are emerging as a prominent tool to produce continuous and uniform films of 2D nanomaterials on various substrates (*e.g.* steel sheet, titanium sheet, and carbon foam) for industrial demands.[168] On the other hand, integration of the obtained cost-efficient and activity-intensive 2D nanomaterial into a suitable electrolyzer is considered to be another wise strategy to meet industrial demands. In this regard, a flow electrolyzer shows enormous potential for the continuous production of H_2 and valuable chemicals, benefitting from a number of significant advantages over the batch cell including: (1) higher productivity and yield, (2) better control and optimization of the reaction parameters, (3) easier separation and purification of the products, and (4) lower energy consumption and waste generation.[169] More promisingly, employment of several flow electrolyzers in a row will offer a great opportunity to improve the efficiency, selectivity, and scalability of targeting reactions.

Considering the aforementioned challenges and emerging solutions, a schematic representation of the four-gear concept is depicted in Fig. 8, demonstrating how the four interrelated, yet independent parts can form a whole.

4. Conclusion

In summary, this review highlights the design and application of versatile 2D nanomaterials in hybrid water electrolysis technology, which is able to simultaneously produce green H_2 fuels and valuable chemicals/intermediates from naturally abundant biomass feedstocks. Specifically, this review provides a comprehensive summary of recently developed design strategies (including benefits, limitations and complementary strategies) for functional nanostructured 2D (photo-)electrocatalysts for the HMFOR, GOR or LOR coupled with the HER. A thorough literature survey reveals that, benefiting from rational design strategies, the enhanced physical and chemical properties of 2D nanomaterials largely facilitate hybrid water electrolysis performance. Notably, it is crucial to address the current challenges related to intelligent design toward next-generation 2D nanostructured electrocatalysts, insightful (photo-)electrochemical surface investigation under operation, sustainable recovery and regeneration of active species after service, and industrially relevant scaling-up applications. Addressing these practical issues provides a great opportunity to advance hybrid water (photo-)electrolysis technology towards higher efficiency and lower cost.

Data availability

This review article does not present any new data analyzed by the authors. All data discussed in this review are derived from previously published studies with the respective citation in the text. Additional ESI data† and comparison tables have been included, which are cited accordingly within the ESI.†

Author contributions

B. F. M. and D. G. conceived the idea for the review. The manuscript was written and reviewed through contributions of all authors. All authors have given approval to the final version of the manuscript.

Conflicts of interest

The authors declare no conflict of interests.

Acknowledgements

B. F. M. acknowledges the Alexander-von-Humboldt-Foundation for a postdoctoral fellowship (project no. 1231127). Johannes Gutenberg University Mainz is gratefully

acknowledged for financial support. D. G. acknowledges the Deutsche Forschungsgemeinschaft (DFG) for a Walter Benjamin Fellowship (project no. 510966757). D. G. gratefully acknowledges the financial support by the Carl Zeiss Foundation (Halocycles no P2021-10-007). D. G. gratefully acknowledges funding from the Top Level Research Area SusInnoScience of the federal state of Rheinland-Pfalz.

Notes and references

1 M. Faraji, M. Yousefi, S. Yousefzadeh, M. Zirak, N. Naseri, T. H. Jeon, W. Choi and A. Z. Moshfegh, *Energy Environ. Sci.*, 2019, **12**, 59–95.
2 Y. S. Park, J. Yang, J. Lee, M. J. Jang, J. Jeong, W.-S. Choi, Y. Kim, Y. Yin, M. H. Seo and Z. Chen, *Appl. Catal., B*, 2020, **278**, 119276.
3 N.-T. Suen, S.-F. Hung, Q. Quan, N. Zhang, Y.-J. Xu and H. M. Chen, *Chem. Soc. Rev.*, 2017, **46**, 337–365.
4 S. Anantharaj, S. R. Ede, K. Sakthikumar, K. Karthick, S. Mishra and S. Kundu, *ACS Catal.*, 2016, **6**, 8069–8097.
5 A. Raveendran, M. Chandran and R. Dhanusuraman, *RSC Adv.*, 2023, **13**, 3843–3876.
6 J. E. Lee, K.-J. Jeon, P. L. Show, S.-C. Jung, Y. J. Choi, G. H. Rhee, K.-Y. A. Lin and Y.-K. Park, *Fuel*, 2022, **308**, 122048.
7 L. Wang, Y. Tong, J. Feng, J. Hou, J. Li, X. Hou and J. Liang, *Sustainable Mater. Technol.*, 2019, **19**, e00089.
8 X. Li, R. Shen, S. Ma, X. Chen and J. Xie, *Appl. Surf. Sci.*, 2018, **430**, 53–107.
9 J. Yi, W. El-Alami, Y. Song, H. Li, P. M. Ajayan and H. Xu, *Chem. Eng. J.*, 2020, **382**, 122812.
10 H. Zhou, F. Yu, Q. Zhu, J. Sun, F. Qin, L. Yu, J. Bao, Y. Yu, S. Chen and Z. Ren, *Energy Environ. Sci.*, 2018, **11**, 2858–2864.
11 T. Naito, T. Shinagawa, T. Nishimoto and K. Takanabe, *Inorg. Chem. Front.*, 2021, **8**, 2900–2917.
12 C. C. L. McCrory, S. Jung, J. C. Peters and T. F. Jaramillo, *J. Am. Chem. Soc.*, 2013, **135**, 16977–16987.
13 X. Xie, L. Du, L. Yan, S. Park, Y. Qiu, J. Sokolowski, W. Wang and Y. Shao, *Adv. Funct. Mater.*, 2022, **32**, 2110036.
14 X. Liu, Y. Ji, G. Chen, X. Peng, L. Yi, J. Chen, X. Feng and Z. Wen, *Small Struct.*, 2021, **2**, 2100121.
15 B. You, X. Liu, X. Liu and Y. Sun, *ACS Catal.*, 2017, **7**, 4564–4570.
16 K. Xiang, D. Wu, X. Deng, M. Li, S. Chen, P. Hao, X. Guo, J. L. Luo and X. Z. Fu, *Adv. Funct. Mater.*, 2020, **30**, 1909610.
17 W.-J. Liu, L. Dang, Z. Xu, H.-Q. Yu, S. Jin and G. W. Huber, *ACS Catal.*, 2018, **8**, 5533–5541.
18 B. You, X. Liu, N. Jiang and Y. Sun, *J. Am. Chem. Soc.*, 2016, **138**, 13639–13646.
19 C. Lamy, A. Devadas, M. Simoes and C. Coutanceau, *Electrochim. Acta*, 2012, **60**, 112–120.
20 W. Guo, L. Li, L. Li, S. Tian, S. Liu and Y. Wu, *Int. J. Hydrogen Energy*, 2011, **36**, 9415–9419.
21 Y. Huang, X. Chong, C. Liu, Y. Liang and B. Zhang, *Angew. Chem., Int. Ed.*, 2018, **130**, 13347–13350.
22 S. Xue, S. Watzele, V. Čolić, K. Brandl, B. Garlyyev and A. S. Bandarenka, *ChemSusChem*, 2017, **10**, 4812–4816.
23 W. Peng, L. Xiao, B. Huang, L. Zhuang and J. Lu, *J. Phys. Chem. C*, 2011, **115**, 23050–23056.
24 J. Huang, J. Cai and J. Wang, *ACS Appl. Energy Mater.*, 2020, **3**, 4108–4113.
25 J. Y. Zhang, H. Wang, Y. Tian, Y. Yan, Q. Xue, T. He, H. Liu, C. Wang, Y. Chen and B. Y. Xia, *Angew. Chem., Int. Ed.*, 2018, **57**, 7649–7653.
26 P. Babar, A. Lokhande, V. Karade, I. J. Lee, D. Lee, S. Pawar and J. H. Kim, *J. Colloid Interface Sci.*, 2019, **557**, 10–17.
27 X. Zhao, L. Dai, Q. Qin, F. Pei, C. Hu and N. Zheng, *Small*, 2017, **13**, 1602970.
28 J. Zheng, X. Chen, X. Zhong, S. Li, T. Liu, G. Zhuang, X. Li, S. Deng, D. Mei and J. G. Wang, *Adv. Funct. Mater.*, 2017, **27**, 1704169.
29 Z. Fan, W. Zhang, L. Li, Y. Wang, Y. Zou, S. Wang and Z. Chen, *Green Chem.*, 2022, **24**, 7818–7868.
30 H. Luo, J. Barrio, N. Sunny, A. Li, L. Steier, N. Shah, I. E. Stephens and M. M. Titirici, *Adv. Energy Mater.*, 2021, **11**, 2101180.
31 Z. Sun, B. Fridrich, A. De Santi, S. Elangovan and K. Barta, *Chem. Rev.*, 2018, **118**, 614–678.
32 C. Liu, S. Wu, H. Zhang and R. Xiao, *Fuel Process. Technol.*, 2019, **191**, 181–201.
33 M.-I. Jamesh and X. Sun, *J. Power Sources*, 2018, **400**, 31–68.
34 C. Deng, C. Y. Toe, X. Li, J. Tan, H. Yang, Q. Hu and C. He, *Adv. Energy Mater.*, 2022, 2201047.
35 S. Bellani, A. Bartolotta, A. Agresti, G. Calogero, G. Grancini, A. Di Carlo, E. Kymakis and F. Bonaccorso, *Chem. Soc. Rev.*, 2021, 11870–11965.
36 D. Scarano and F. Cesano, *Materials*, 2021, **14**, 7108.
37 C. S. Bongu, S. Tasleem, M. R. Krishnan and E. H. Alsharaeh, *Sustainable Energy Fuels*, 2024, 4039–4070.
38 H. He, L. Guan and H. Le Ferrand, *J. Mater. Chem. A*, 2022, 19129–19168.
39 M. H. Kalantari and X. Zhang, *Nanomaterials*, 2022, **13**, 117.
40 B. Zheng, S. Yu, Z. Chen and Y.-X. Huo, *Front. Microbiol.*, 2022, **13**, 933882.
41 A. Zhang, Y. Liang, H. Zhang, Z. Geng and J. Zeng, *Chem. Soc. Rev.*, 2021, 9817–9844.
42 H. Zhu, X. Gan, A. McCreary, R. Lv, Z. Lin and M. Terrones, *Nano Today*, 2020, **30**, 100829.
43 J. Xie, J. Zhang, S. Li, F. Grote, X. Zhang, H. Zhang, R. Wang, Y. Lei, B. Pan and Y. Xie, *J. Am. Chem. Soc.*, 2013, **135**, 17881–17888.
44 Z. Ning, S. Gan, H. Xu, C. Gu, P. Zhu, J. Zhou and G. Xiao, *J. Mater. Chem. A*, 2024, **12**, 5885–5897.
45 M. Gao, L. Zhu, C. K. Peh and G. W. Ho, *Energy Environ. Sci.*, 2019, **12**, 841–864.
46 J. Li and N. Wu, *Catal. Sci. Technol.*, 2015, **5**, 1360–1384.
47 D. N. Tafen, J. Wang, N. Wu and J. P. Lewis, *Appl. Phys. Lett.*, 2009, **94**, 093101.
48 H. P. Maruska and A. K. Ghosh, *Sol. Energy Mater.*, 1979, **1**, 237–247.
49 J. M. Luther, P. K. Jain, T. Ewers and A. P. Alivisatos, *Nat. Mater.*, 2011, **10**, 361–366.

50 T. Wei, W. Liu, S. Zhang, Q. Liu, J. Luo and X. Liu, *Chem. Commun.*, 2023, **59**, 442–445.
51 J. Zhang, P. Yu, G. Zeng, F. Bao, Y. Yuan and H. Huang, *J. Mater. Chem. A*, 2021, **9**, 9685–9691.
52 D. Li, Y. Huang, Z. Li, L. Zhong, C. Liu and X. Peng, *J. Chem. Eng.*, 2022, **430**, 132783.
53 D. Li, Z. Li, R. Zou, G. Shi, Y. Huang, W. Yang, W. Yang, C. Liu and X. Peng, *Appl. Catal., B*, 2022, **307**, 121170.
54 T. Cui, L. Ma, S. Wang, C. Ye, X. Liang, Z. Zhang, G. Meng, L. Zheng, H.-S. Hu and J. Zhang, *J. Am. Chem. Soc.*, 2021, **143**, 9429–9439.
55 X. Hao, Y. Quansheng, S. Dan, Y. Honghui, L. Jidong, F. Jiangtao and Y. Wei, *J. Hazard. Mater.*, 2015, **286**, 509–516.
56 C. Zhao, Z. Li, T. Fan, C. Xiao and Y. Xie, *Research*, 2020, **2020**, 652749.
57 X. Yan, L. Zhuang, Z. Zhu and X. Yao, *Nanoscale*, 2021, **13**, 3327–3345.
58 T. Tang, Z. Wang and J. Guan, *Chin. J. Catal.*, 2022, **43**, 636–678.
59 D. Maarisetty and S. S. Baral, *J. Mater. Chem. A*, 2020, **8**, 18560–18604.
60 J. Yan, G. Wu, N. Guan, L. Li, Z. Li and X. Cao, *Phys. Chem. Chem. Phys.*, 2013, **15**, 10978–10988.
61 M. Xu, X. Ruan, D. Meng, G. Fang, D. Jiao, S. Zhao, Z. Liu, Z. Jiang, K. Ba, T. Xie, W. Zhang, J. Leng, S. Jin, S. K. Ravi and X. Cui, *Adv. Funct. Mater.*, 2024, 2402330.
62 B. Zhang, Z. Yang, C. Yan, Z. Xue and T. Mu, *Small*, 2023, **19**, 2207236.
63 B. Zhu, Y. Qin, J. Du, F. Zhang and X. Lei, *ACS Sustain. Chem. Eng.*, 2021, **9**, 11790–11797.
64 Z. Tian, Y. Da, M. Wang, X. Dou, X. Cui, J. Chen, R. Jiang, S. Xi, B. Cui and Y. Luo, *Nat. Commun.*, 2023, **14**, 142.
65 J. Yang, D. Wang, H. Han and C. Li, *Acc. Chem. Res.*, 2013, **46**, 1900–1909.
66 M. Kumar, B. Meena, P. Subramanyam, D. Suryakala and C. Subrahmanyam, *NPG Asia Mater.*, 2022, **14**, 88.
67 X. T. Xu, L. Pan, X. Zhang, L. Wang and J. J. Zou, *Adv. Sci.*, 2019, **6**, 1801505.
68 H. Wang, L. Zhang, Z. Chen, J. Hu, S. Li, Z. Wang, J. Liu and X. Wang, *Chem. Soc. Rev.*, 2014, **43**, 5234–5244.
69 H. Hou, X. Zeng and X. Zhang, *Sci. China Mater.*, 2020, **63**, 2119–2152.
70 S. Liang, L. Pan, T. Thomas, B. Zhu, C. Chen, J. Zhang, H. Shen, J. Liu and M. Yang, *J. Chem. Eng.*, 2021, **415**, 128864.
71 S. Wang, X. Gao, X. Hang, X. Zhu, H. Han, X. Li, W. Liao and W. Chen, *J. Am. Chem. Soc.*, 2018, **140**, 6271–6277.
72 D. Rauber, T. K. Dier, D. A. Volmer and R. Hempelmann, *Z. Phys. Chem.*, 2018, **232**, 189–208.
73 J. Miao, Y. Ma, X. Wang, Y. Li, H. Wang, L. Zhang, J. Zhang, Y. Qin and J. Gao, *Appl. Catal., B*, 2023, 122937.
74 H. Wang, W. Fu, X. Yang, Z. Huang, J. Li, H. Zhang and Y. Wang, *J. Mater. Chem. A*, 2020, **8**, 6926–6956.
75 X. Ruan, S. Li, C. Huang, W. Zheng, X. Cui and S. K. Ravi, *Adv. Mater.*, 2024, **36**, 2305285.
76 P. Solís-Fernández, M. Bissett and H. Ago, *Chem. Soc. Rev.*, 2017, **46**, 4572–4613.
77 X. Du, J. Huang, J. Zhang, Y. Yan, C. Wu, Y. Hu, C. Yan, T. Lei, W. Chen and C. Fan, *Angew. Chem., Int. Ed.*, 2019, **58**, 4484–4502.
78 X. Wu, Y. Wang and Z.-S. Wu, *Chem*, 2022, 13170–13189.
79 J. Low, S. Cao, J. Yu and S. Wageh, *Chem. Commun.*, 2014, **50**, 10768–10777.
80 J. Su, G. D. Li, X. H. Li and J. S. Chen, *Adv. Sci.*, 2019, **6**, 1801702.
81 X. Li and J. Wang, *InfoMat*, 2020, **2**, 3–32.
82 Q. Wei, F. Xiong, S. Tan, L. Huang, E. H. Lan, B. Dunn and L. Mai, *Adv. Mater.*, 2017, **29**, 1602300.
83 Y. Li, M. Ma, D. Yi, Q. Zhou, J. Chen, Y. Bian, W. Niu, C. Yang, Z. Yin, Z. Wang and A. Tang, *Adv. Funct. Mater.*, 2024, 2407271.
84 L. Zhang, J. Zhang, H. Yu and J. Yu, *Adv. Mater.*, 2022, **34**, 2107668.
85 Q. Xu, L. Zhang, B. Cheng, J. Fan and J. Yu, *Chem*, 2020, **6**, 1543–1559.
86 M. Sun, J. Yang, J. Huang, Y. Wang, X. Liu, Y. Qi and L. Zhang, *Langmuir*, 2023, **39**, 3762–3769.
87 Y. Zhong, R.-Q. Ren, J.-B. Wang, Y.-Y. Peng, Q. Li and Y.-M. Fan, *Catal. Sci. Technol.*, 2022, **12**, 201–211.
88 X. Deng, X. Kang, M. Li, K. Xiang, C. Wang, Z. Guo, J. Zhang, X.-Z. Fu and J.-L. Luo, *J. Mater. Chem. A*, 2020, **8**, 1138–1146.
89 F. Sun, Y. Zhou, Z. You, H. Xia, Y. Tuo, S. Wang, C. Jia and J. Zhang, *Small*, 2021, **17**, 2103307.
90 F. Bateni, M. NaderiNasrabadi, R. Ghahremani and J. A. Staser, *J. Electrochem. Soc.*, 2019, **166**, F1037.
91 M. NaderiNasrabadi, F. Bateni, Z. Chen, P. B. Harrington and J. A. Staser, *J. Electrochem. Soc.*, 2019, **166**, E317.
92 Y. Hu, H. Huang, J. Feng, W. Wang, H. Guan, Z. Li and Z. Zou, *Sol. RRL*, 2021, **5**, 2100100.
93 F. E. Osterloh, *Chem. Soc. Rev.*, 2013, **42**, 2294–2320.
94 Y. Zhou, L. Zhang, L. Lin, B. R. Wygant, Y. Liu, Y. Zhu, Y. Zheng, C. B. Mullins, Y. Zhao and X. Zhang, *Nano Lett.*, 2017, **17**, 8012–8017.
95 M. Bae, Y. Kang, D. W. Lee, D. Jeon and J. Ryu, *Adv. Energy Mater.*, 2022, **12**, 2201452.
96 X. Deng, M. Li, Y. Fan, L. Wang, X.-Z. Fu and J.-L. Luo, *Appl. Catal., B*, 2020, **278**, 119339.
97 C. Sun, D. Zhang, Y. Zhao, C. Song and D. Wang, *Colloids Surf., A*, 2022, **650**, 129597.
98 Z. Zhou, C. Chen, M. Gao, B. Xia and J. Zhang, *Green Chem.*, 2019, **21**, 6699–6706.
99 Y. Wang, W. Yan, M. Ni, C. Zhu and H. Du, *Chem. Commun.*, 2023, **59**, 2485–2488.
100 R. Ghahremani, F. Farales, F. Bateni and J. A. Staser, *J. Electrochem. Soc.*, 2020, **167**, 043502.
101 K. Jakubow-Piotrowska, B. Witkowski and J. Augustynski, *Commun. Chem.*, 2022, **5**, 125.
102 Y. Xue, G. Zhao, R. Yang, F. Chu, J. Chen, L. Wang and X. Huang, *Nanoscale*, 2021, **13**, 3911–3936.
103 L. P. Lefebvre, J. Banhart and D. C. Dunand, *Adv. Eng. Mater.*, 2008, **10**, 775–787.

104 W. Zhu, R. Zhang, F. Qu, A. M. Asiri and X. Sun, *ChemCatChem*, 2017, **9**, 1721–1743.
105 C. Körner and R. F. Singer, *Adv. Eng. Mater.*, 2000, **2**, 159–165.
106 D. Gao, R. Liu, S. Liu, S. Greiner, M. Anjass, J. Biskupek, U. Kaiser, H. Braun, T. Jacob and C. Streb, *ACS Appl. Mater. Interfaces*, 2021, **13**, 19048–19054.
107 D. Gao, R. Liu, J. Biskupek, U. Kaiser, Y. F. Song and C. Streb, *Angew. Chem., Int. Ed.*, 2019, **58**, 4644–4648.
108 F. Chen, C. Chen, Q. Hu, B. Xiang, T. Song, X. Zou, W. Li, B. Xiong and M. Deng, *J. Chem. Eng.*, 2020, **401**, 126145.
109 R. Zhang, J. Liu, H. Guo and X. Tong, *Mater. Lett.*, 2015, **139**, 55–58.
110 D. Gao, S. Liu, R. Liu and C. Streb, *Chem.–Eur. J.*, 2020, **26**, 11109–11112.
111 C. Chen, Z. Zhou, J. Liu, B. Zhu, H. Hu, Y. Yang, G. Chen, M. Gao and J. Zhang, *Appl. Catal., B*, 2022, **307**, 121209.
112 Y. Xie, L. Sun, X. Pan, Z. Zhou and G. Zhao, *Appl. Catal., B*, 2023, **338**, 123068.
113 Y. Xin, F. Wang, L. Chen, Y. Li and K. Shen, *Green Chem.*, 2022, **24**, 6544–6555.
114 N. Wang, R. Xue, N. Yang, H. Sun, B. Zhang, Z. Ma, Y. Ma and L. Zang, *J. Alloys Compd.*, 2022, **929**, 167324.
115 W.-J. Liu, Z. Xu, D. Zhao, X.-Q. Pan, H.-C. Li, X. Hu, Z.-Y. Fan, W.-K. Wang, G.-H. Zhao, S. Jin, G. W. Huber and H.-Q. Yu, *Nat. Commun.*, 2020, **11**, 265.
116 M. Garedew, F. Lin, B. Song, T. M. DeWinter, J. E. Jackson, C. M. Saffron, C. H. Lam and P. T. Anastas, *ChemSusChem*, 2020, **13**, 4214–4237.
117 M. Zirbes, D. Schmitt, N. Beiser, D. Pitton, T. Hoffmann and S. R. Waldvogel, *ChemElectroChem*, 2019, **6**, 155–161.
118 Z. Fang, J. E. Jackson and E. L. Hegg, *ACS Sustain. Chem. Eng.*, 2022, **10**, 7545–7552.
119 D. Schmitt, C. Regenbrecht, M. Hartmer, F. Stecker and S. R. Waldvogel, *Beilstein J. Org. Chem.*, 2015, **11**, 473–480.
120 D. Schmitt, C. Regenbrecht, M. Schubert, D. Schollmeyer and S. R. Waldvogel, *Holzforschung*, 2017, **71**, 35–41.
121 M. Breiner, M. Zirbes and S. R. Waldvogel, *Green Chem.*, 2021, **23**, 6449–6455.
122 X. Wang, G. Sun, P. Routh, D.-H. Kim, W. Huang and P. Chen, *Chem. Soc. Rev.*, 2014, **43**, 7067–7098.
123 B. F. Mohazzab, A. Akhundi, K. Rahimi, B. Jaleh and A. Z. Moshfegh, *ACS Appl. Energy Mater.*, 2022, **5**, 12283–12296.
124 S. Mansoor, M. Tayyab, M. Khan, Z. Akmal, L. Zhou, J. Lei, M. Anpo and J. Zhang, *Res. Chem. Intermed.*, 2023, **49**, 3723–3745.
125 A. Kumar, P. Raizada, A. Hosseini-Bandegharaei, V. K. Thakur, V.-H. Nguyen and P. Singh, *J. Mater. Chem. A*, 2021, **9**, 111–153.
126 V. Gurylev and V. Gurylev, *Nanostructured Photocatalyst via Defect Engineering: Basic Knowledge and Recent Advances*, 2021, pp. 37–72.
127 H. L. Chia, C. C. Mayorga-Martinez and M. Pumera, *Adv. Funct. Mater.*, 2021, **31**, 2102555.
128 H. Zheng, Y. Li, H. Liu, X. Yin and Y. Li, *Chem. Soc. Rev.*, 2011, **40**, 4506–4524.
129 X. Sun, L. Shi, H. Huang, X. Song and T. Ma, *Chem. Commun.*, 2020, **56**, 11000–11013.
130 L. Maggini and R. R. Ferreira, *J. Mater. Chem. C*, 2021, **9**, 15721–15734.
131 C. Feng, Z.-P. Wu, K.-W. Huang, J. Ye and H. Zhang, *Adv. Mater.*, 2022, **34**, 2200180.
132 Y. Wu and N. Liu, *Chem*, 2018, **4**, 438–465.
133 K. Zhu, X. Zhu and W. Yang, *Angew. Chem., Int. Ed.*, 2019, **58**, 1252–1265.
134 A. Preet and T.-E. Lin, *Catalysts*, 2021, **11**, 594.
135 N. Ortiz Peña, D. Ihiawakrim, M. Han, B. Lassalle-Kaiser, S. Carenco, C. Sanchez, C. Laberty-Robert, D. Portehault and O. Ersen, *ACS Nano*, 2019, **13**, 11372–11381.
136 P. Su, V. Prabhakaran, G. E. Johnson and J. Laskin, *Anal. Chem.*, 2018, **90**, 10935–10942.
137 T. Faverge, B. Gilles, A. Bonnefont, F. Maillard, C. Coutanceau and M. Chatenet, *ACS Catal.*, 2023, **13**, 2657–2669.
138 D.-J. Chen and Y. Tong, *Chem. Commun.*, 2015, **51**, 5683–5686.
139 S.-i. Ogino, T. Itoh, D. Mabuchi, K. Yokoyama, K. Motomiya, K. Tohji and Y. Sato, *J. Phys. Chem. C*, 2016, **120**, 7133–7143.
140 Y.-H. Wang, S. Li, R.-Y. Zhou, S. Zheng, Y.-J. Zhang, J.-C. Dong, Z.-L. Yang, F. Pan, Z.-Q. Tian and J.-F. Li, *Nat. Protoc.*, 2023, **18**, 883–901.
141 D. Chen, Y. Ding, X. Cao, L. Wang, H. Lee, G. Lin, W. Li, G. Ding and L. Sun, *Angew. Chem., Int. Ed.*, 2023, **62**, e202309478.
142 N. Zhang, Y. Zou, L. Tao, W. Chen, L. Zhou, Z. Liu, B. Zhou, G. Huang, H. Lin and S. Wang, *Angew. Chem., Int. Ed.*, 2019, **131**, 16042–16050.
143 R. De and B. Dietzek-Ivanšić, *Chem.–Eur. J.*, 2022, **28**, e202200407.
144 A. Kemna, N. García Rey and B. Braunschweig, *ACS Catal.*, 2019, **9**, 6284–6292.
145 J. Timoshenko and B. Roldan Cuenya, *Chem. Rev.*, 2020, **121**, 882–961.
146 M. Risch, D. M. Morales, J. Villalobos and D. Antipin, *Angew. Chem., Int. Ed.*, 2022, **61**, e202211949.
147 S. Chen, L. Ma, Z. Huang, G. Liang and C. Zhi, *Cell Rep. Phys. Sci.*, 2022, 100729.
148 N. Gupta, C. Segre, C. Nickel, C. Streb, D. Gao and K. D. Glusac, *ACS Appl. Mater. Interfaces*, 2024, **16**, 35793–35804.
149 C.-J. Chang, Y. Zhu, J. Wang, H.-C. Chen, C.-W. Tung, Y.-C. Chu and H. M. Chen, *J. Mater. Chem. A*, 2020, **8**, 19079–19112.
150 Y. Zhu, T.-R. Kuo, Y.-H. Li, M.-Y. Qi, G. Chen, J. Wang, Y.-J. Xu and H. M. Chen, *Energy Environ. Sci.*, 2021, **14**, 1928–1958.
151 K. A. Stoerzinger, W. T. Hong, E. J. Crumlin, H. Bluhm and Y. Shao-Horn, *Acc. Chem. Res.*, 2015, **48**, 2976–2983.
152 Y.-D. Cao, W.-X. Mu, M. Gong, L.-L. Fan, J. Han, H. Liu, B. Qi and G.-G. Gao, *Dalton Trans.*, 2023, 7343–7350.
153 J. K. Nørskov, F. Abild-Pedersen, F. Studt and T. Bligaard, *Proc. Natl. Acad. Sci. U. S. A.*, 2011, **108**, 937–943.

154 Y.-K. Lee, *Catalysts*, 2021, **11**, 454.
155 Z. W. Seh, J. Kibsgaard, C. F. Dickens, I. Chorkendorff, J. K. Nørskov and T. F. Jaramillo, *Science*, 2017, **355**, eaad4998.
156 L. Ostervold, S. I. P. Bakovic, J. Hestekin and L. F. Greenlee, *RSC Adv.*, 2021, **11**, 31208–31218.
157 M. G. Kibria, N. I. Masuk, R. Safayet, H. Q. Nguyen and M. Mourshed, *Int. J. Environ. Res.*, 2023, **17**, 20.
158 S. Cheng, L. Wei, X. Zhao and J. Julson, *Catalysts*, 2016, **6**, 195.
159 I. V. Yentekakis and F. Dong, *Front. Environ. Chem.*, 2020, **5**, 1–5.
160 C. H. Bartholomew and M. D. Argyle, *Catalysts*, 2015, **5**, 949–954.
161 X. Zhang, S. Xu, J. Tang, L. Fu and H. Karimi-Maleh, *Catalysts*, 2022, **12**, 818.
162 L. X. Chen, Z. W. Chen, M. Jiang, Z. Lu, C. Gao, G. Cai and C. V. Singh, *J. Mater. Chem. A*, 2021, **9**, 2018–2042.
163 K. Khan, A. K. Tareen, M. Aslam, R. U. R. Sagar, B. Zhang, W. Huang, A. Mahmood, N. Mahmood, K. Khan and H. Zhang, *Nano-Micro Lett.*, 2020, **12**, 1–77.
164 N. Rohaizad, C. C. Mayorga-Martinez, M. Fojtů, N. M. Latiff and M. Pumera, *Chem. Soc. Rev.*, 2021, **50**, 619–657.
165 H. Sun, X. Xu, H. Kim, W. Jung, W. Zhou and Z. Shao, *Energy Environ. Mater.*, 2022, e12441.
166 W. Li, H. Tian, L. Ma, Y. Wang, X. Liu and X. Gao, *Mater. Adv.*, 2022, **3**, 5598–5644.
167 S. H. Choi, S. J. Yun, Y. S. Won, C. S. Oh, S. M. Kim, K. K. Kim and Y. H. Lee, *Nat. Commun.*, 2022, **13**, 1484.
168 E. S. Polsen, D. Q. McNerny, B. Viswanath, S. W. Pattinson and A. John Hart, *Sci. Rep.*, 2015, **5**, 1–12.
169 D. Pollok and S. R. Waldvogel, *Chem. Sci.*, 2020, **11**, 12386–12400.